PHYSICAL REVIEW B VOLUME 4, NUMBER 6 15 SEPTEMBER 1971

X-Ray Scattering from hcp Crystals Containing Interstitial Basal-Plane Loops*

D. T. Keating and A. N. Goland
Brookhaven National Laboratory, Upton, New York 11973
(Received 7 May 1971)

The diffraction effects arising from the presence of interstitial basal-plane loops in an ideal hcp crystal are analyzed using a high-speed computer. The atomic displacements were computed assuming that the crystal responds to the loop as an isotropic elastic medium with a Poisson's ratio of 0.3 into which a "penny-shaped" inclusion is inserted. The loops are assumed to be circular clusters of atoms in the C position of the normal $ABAB\cdots$ sequence of hcp planes. The resulting defect is a finite extrinsic fault and its associated strain field. The effects of loop size and concentration on the lattice parameters, Bragg intensities, and diffuse scattering are given. Graphs are presented which allow the determination of loop size and concentration from the measurement of lattice parameters and Bragg intensities. Isodiffusion contour maps of the diffuse scattering in the $(HH\cdot L)$ and $(HO\cdot L)$ planes of reciprocal space are presented. The diffuse scattering around reciprocal-lattice points for which $H-K=$ modulo 3 is quite different from that around reciprocal-lattice points for which $H-K\neq$ modulo 3. The former depends strongly on the symmetry of the loop strain field and is concentrated around the reciprocal-lattice point, while the latter reflects more strongly the disruption of the stacking sequence, having characteristically S-shaped streaks connecting the reciprocal-lattice points. The size of the loops can be determined approximately from the full width at half-maximum of the streak connecting the $(10\cdot 0)$ and $(10\cdot 1)$ reflections. The diffraction effects produced by basal-plane loops are discussed in connection with those seen in neutron-irradiated BeO. All of the predicted effects are seen in neutron-irradiated BeO, including the duplex nature of the reflections with $L\neq 0$ and the crosses around reciprocal-lattice points for which $H-K=$ modulo 3 and $L=0$.

I. INTRODUCTION

It is now generally recognized that the spherically symmetric displacement field often assumed for point defects is incapable of explaining the scattering effects observed in irradiated solids. It is generally believed that more complicated point defects, such as split interstitials,[1,2] are formed in irradiated solids. If the point defects can migrate to form clusters, then even more complicated defects can result.[3] In BeO irradiated by neutrons at high temperatures, large interstitial basal-plane dislocation loops are observed with the electron microscope.[4-6] However, clusters can be so small that the nature of the defect cannot always be determined by transmission electron microscopy, and diffraction effects provide information about the nature of the defect. The authors have investigated the x-ray scattering from doublet singularities produced by the carbon interstitial in iron.[7,8] It was a natural extension of these studies that led us to examine the effects of prismatic dislocation loops on the x-ray scattering.

In this paper we direct our attention specifically to the condensation of interstitial atoms into the C position between the normal $ABAB\cdots$ sequence of hcp basal planes. The defect is then a finite extrinsic fault and its associated strain field. Although faulting disorders have been extensively treated in the literature[9-12] it is always assumed, with one exception,[13] that the fault extends across the whole plane in the crystal. Such an approach cannot account for the finite size of the fault nor for the strain field of the prismatic dislocation loop. Several investigators have alluded to these failings in considering similar problems.[14,15] The diffraction effects produced by extrinsic faults in hcp structures were first considered by Sabine[16] and later by Lele *et al.*[17] The methods employed in these two papers are quite different but the predicted scattering effects agree to first order in the faulting parameter. However, our results differ substantially from these predictions, a fact which we attribute to the finite nature of the faults in our case. To our knowledge, no one has formulated the scattering by taking into account both the finite nature of the fault and the strain field produced by the prismatic dislocation loop. Krivoglaz and Ryaboshapka have treated the most general loop[18,19] using the displacement field for the "infinitesimal" loop (the field at large distances from a loop[20]), but neglecting the scattering effects of the finite fault. We have found the displacements around a prismatic dislocation loop in an elastic isotropic medium at all distances[21,22] and these results are used in this paper. These results are applicable to interstitial loops in both fcc and hcp structures and vacancy loops in fcc structures.

We review briefly the assumptions that were used in calculating the displacement field, and then treat the effects on the Bragg intensities, lattice parameters, and diffuse scattering that result from the presence of dislocation loops. We treat the attenu-

ation of the Bragg intensities by a method first introduced by Krivoglaz.[23,24] The usual artificial temperature factor employing the mean square static displacement[25] is inadequate because the displacements produced by a dislocation loop are large. The reduction in intensities caused by the loop displacements dominates those changes in the average structure factor arising from the loops. The change in lattice parameters is deduced from the total displacement field produced by the loops, which is the sum of the displacement field produced by the defects in an infinite medium and the so-called image field.[26,27] The displacement field at large distances from a loop is the sum of the displacement fields from a point and doublet singularity, the strengths of which are determined by the number of atoms in the loop.[21,22] We use an expression for the diffuse scattering which is interpreted—in terms of the Fourier transform of the loop considered—as the origin and the difference between the amplitude scattered by the atoms surrounding the loop in their displaced and undisplaced positions.[28–34] We assume that the interaction between different loops is negligible. Throughout this paper, the principle of superposition is assumed to be valid.

We emphasize those aspects of the diffraction phenomena which give information about loop size and concentration. Graphs are given which enable one to determine loop size and concentration from measurements of lattice parameters and Bragg intensities. Under favorable conditions it is also possible to obtain this information from the diffuse scattering. Finally, these diffraction effects are discussed in connection with experimental observations on neutron-irradiated BeO.

II. DISPLACEMENT FIELD

The atomic displacements in our crystal resulting from an interstitial dislocation loop were assumed to be those that would result from considering the following model: We inscribe in an isotropic elastic medium with a Poisson's ratio of 0.3 a hcp network of points representing the atoms of our crystal. The vectors of the unit cell are $\vec{A}_1$, $\vec{A}_2$, and $\vec{A}_3$, and $A_3/A_1=\sqrt{\frac{8}{3}}$, that of the ideal hcp structure. Imagine that a circular incision of radius c centered on a C position midway between a sequence of $ABAB\cdots$ planes is made in the medium. A disk of thickness b and radius c representing a circular plane of atoms is inserted into the incision and welded to the medium. We imagine that the center of the disk contains an atom and serves as the origin of our coordinate system, and that all other atoms in the disk also lie in the C stacking sequence. We recognize $\vec{b}$ as the Burgers vector, and assume that the atomic displacements in our crystal are those of the points inscribed in our elastic medium.

The problem in elasticity which is to be solved involves deformations which are symmetric about an axis of revolution, and the cylindrical coordinates r, θ, and z are most applicable. In such a symmetrical system the displacement vector and stress tensor are independent of θ. The problem can be solved[21,35,36] by using the methods outlined by Sneddon.[37] Four constants of integration arise which are determined by the boundary conditions. Two of these constants are required to be zero in order that the displacements at large distances from the loop tend to zero. In order that the shear stress not have a discontinuity across the loop plane $z=0$, it must vanish across the entire plane. Further, we require that the z component of the displacements within the loop be half the Burgers vector. These conditions are sufficient to determine uniquely the displacements and stresses.

In terms of the dimensionless variables $\rho=r/c$ and $\zeta=z/c$, the r and z components of the displacements in units of half the Burgers vector are[21]

$$\mu_r^\infty(\rho,\zeta)=-\frac{1}{2(1-\sigma)}\left[(1-2\sigma)I_{11}^0(\rho,\zeta)-\zeta I_{11}^1(\rho,\zeta)\right], \tag{1a}$$

$$\mu_z^\infty(\rho,\zeta)=\frac{1}{2(1-\sigma)}\left[2(1-\sigma)I_{01}^0(\rho,\zeta)+\zeta I_{01}^1(\rho,\zeta)\right], \tag{1b}$$

where σ is Poisson's ratio. The superscript ∞ implies the displacement field in a truly infinite medium and does not include the image displacement field present in a finite medium. The functions I_{mn}^l are integrals of products of mth- and nth-order Bessel functions of the first kind.[21] Figure 1(a) is a contour plot of $\mu_r^\infty(\rho,\zeta)$. The contour interval is 0.02 and the square-grid lines are in units of 0.5 in ρ and ζ. The displacements outward along r are plotted as solid contours whereas those inward are shown as short dashes. The displacements vanish on the long-dashed line. The reader's attention is directed to the fact that within the loop all the displacements are directed inward along r, i.e., the loop itself shrinks in size. Figure 1(b) is a similar plot of $\mu_z^\infty(\rho,\zeta)$; here the contour interval is 0.05, and the grid lines are the same as in Fig. 1(a). All z displacements have the same sign as z, and are largest directly above the loop, forming a pillar of displaced material.

At this point in the problem we encounter a situation which must be resolved in order to formulate the expressions for the attenuation factor and diffuse scattering. Although we think of the loops as always forming in the C position of the stacking sequence, there are two possible ways the loop may appear in the sequence, namely, as $ABACBA\cdots$ or $ABCABA\cdots$. We note that these two defects both have the point-group symmetry $\bar{3}$, and are related

to each other by a rotation of $\frac{2}{6}\pi$. We will refer to the two defects as AB or BA loops, respectively, and consider them to be equally likely. If we index the planes with an index n, with $n=0$ for the first plane above the loop, then the planes with n even are A planes above a BA loop and B planes above an AB loop. The values of the dimensionless coordinates ρ and ζ at any atomic position are

$$\rho(l_1, l_2, n) = (A_1/c)\{[l_1 + \tfrac{1}{6}(3 \pm (-1)^n)]^2 + [l_2 + \tfrac{1}{6}(3 \mp (-1)^n)]^2 - [l_1 + \tfrac{1}{6}(3 \pm (-1)^n)][l_2 + \tfrac{1}{6}(3 \mp (-1)^n)]\}^{1/2} \quad (2a)$$

and

$$\zeta(n) = (A_3/c)\,\tfrac{1}{4}(2n+1)\ . \quad (2b)$$

The integers l_1, l_2, and n have been selected so as to appropriately define the position of an atom in terms of the unit-cell vectors $\vec{A}_1$, $\vec{A}_2$, and $\vec{A}_3$. The top signs are to be used if the loop is an AB loop and the bottom signs if a BA loop.

It is necessary to have the components of the atomic displacements in terms of the unit-cell vectors. Consider the displacement $\mu_r^\infty(\rho, \zeta)$ at the point $\rho(l_1, l_2, n)$ and $\zeta(n)$. To resolve the displacement in the $\vec{A}_1\vec{A}_2$ plane into its components along $\vec{A}_1$ and $\vec{A}_2$, we notice that $\rho(l_1, l_2, n)$ and $\mu_r^\infty(\rho, \zeta)$ lie in the same direction, so that the resolution triangle and position triangle are similar triangles. The displacements in terms of $\vec{A}_1$, $\vec{A}_2$, and $\vec{A}_3$ are then

$$\vec{\mu}^\infty_{A_1}(l_1, l_2, n) = \frac{l_1 + \frac{1}{6}(3 \pm (-1)^n)}{4\rho(l_1, l_2, n)} \frac{A_3}{A_1}\, \mu_r^\infty(\rho, \zeta)\vec{A}_1\ , \quad (3a)$$

$$\vec{\mu}^\infty_{A_2}(l_1, l_2, n) = \frac{l_2 + \frac{1}{6}(3 \mp (-1)^n)}{4\rho(l_1, l_2, n)} \frac{A_3}{A_1}\, \mu_r^\infty(\rho, \zeta)\vec{A}_2\ , \quad (3b)$$

$$\vec{\mu}^\infty_{A_3}(l_1, l_2, n) = \tfrac{1}{4}\,\mu_z^\infty(\rho, \zeta)\vec{A}_3\ . \quad (3c)$$

We have used the relation for half the Burgers vector $\frac{1}{2}\vec{b} = \frac{1}{4}\vec{A}_3$.

III. CHANGE IN LATTICE PARAMETERS

If we have interstitial loops distributed at random in an infinite elastic medium, the displacement of any point is the sum of the displacements from each loop (superposition approximation). If we remove from the infinite medium a finite portion, there is an additional dilatation due to the fact that the infinite portion is no longer acting on our finite portion. This is referred to as the image dilatation.[26,27] The displacement of any point in our finite medium is the sum of the displacement of the point in the infinite medium plus its image displacement. At large distances from our loop the displacements are those produced by a point and doublet singularity, the strengths of which are determined by the number of atoms in the loop. We have discussed this for an isotropic medium, and the fractional changes in lattice parameters are the bulk strains.[21,22] The results are

$$\Delta A_1/A_1 = \Delta A_2/A_2 = 0\ , \quad (4a)$$

$$\Delta A_3/A_3 = p(1 + V_c/V_L)\ , \quad (4b)$$

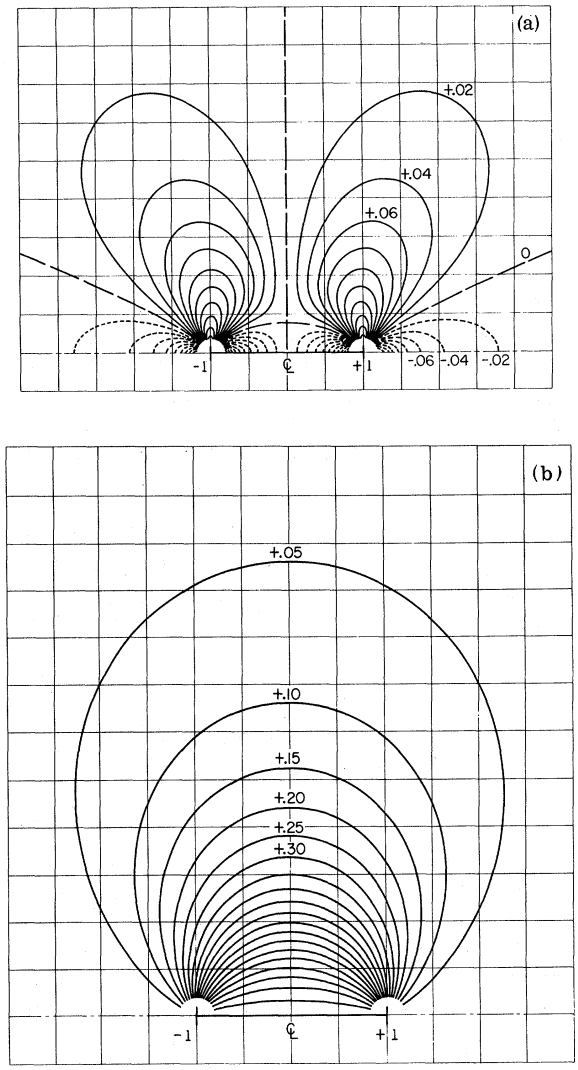

FIG. 1. (a) Contour plot of the r displacements in units of half the Burgers vector. The contour interval is 0.02 and the grid lines are in units of 0.5 in ρ and ζ. The solid contours represent displacements outward along r, and the short dashes displacements inward along r. The zero-displacement contour is a long dash. (b) Contour plot of the z displacements with a contour interval of 0.05.

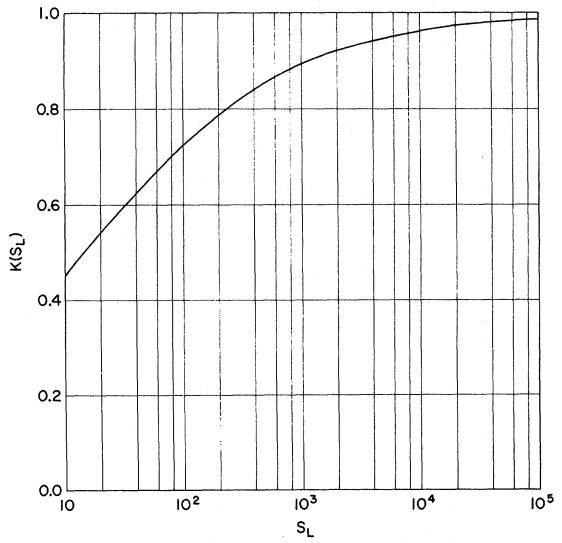

FIG. 2. Plot of $K(S_L)$ vs S_L. For large loops $K(S_L)$ approaches unity.

where p is the fraction of atoms that is present in the form of loops, V_c is the volume of the dislocation core, and V_L is the volume occupied by the atoms in the loop. The estimated value[22] of V_c/V_L is $(8\pi 3^{-1/2} S_L^{-1})^{1/2}$, where S_L is the actual number of atoms in a loop. Thus, if the approximate number of atoms in a loop is known, p can be determined from

$$p = K(S_L)\,\Delta A_3/A_3\,, \tag{5}$$

where $K(S_L) = [1 + (8\pi 3^{-1/2} S_L^{-1})^{1/2}]^{-1}$. A graph of $K(S_L)$ as a function of S_L is given in Fig. 2. For large loops, $K(S_L)$ approaches unity.

IV. ATTENUATION FACTOR

The displacements produced by a dislocation loop are large for extended distances above and below the loop plane, see Fig. 1(b). In this case the expectation value of $e^{i\vec{\kappa}\cdot\vec{\mu}_m}$ need not be $e^{-\langle(\vec{\kappa}\cdot\vec{\mu}_m)^2\rangle/2}$ which is correct for a displacement distribution that is Gaussian and is approximately correct for any distribution as long as $|\vec{\kappa}\cdot\vec{\mu}_m| \ll 1$. Here $\vec{\kappa}$ is the difference in wave vectors of the scattered and incident x-ray beams, and $\vec{\mu}_m$ is the displacement at site m. That is, the usual exponential approximation $e^{-2M'}$ with the artificial temperature factor $2M' = \langle(\vec{\kappa}\cdot\vec{\mu}_m)^2\rangle$ is inadequate. We use the expression first introduced by Krivoglaz[23,24]

$$A_m(\vec{\kappa}) = \prod_j [1 - 4P(1-P)\sin^2(\tfrac{1}{2}\kappa\cdot\mu_{mj})]^{1/2}. \tag{6}$$

$A_m(\vec{\kappa})$ is the factor by which the scattering amplitude of the mth site must be multiplied due to a fractional concentration P of defects, in this case, loops per atom. The displacement of the mth site due to the jth defect is $\vec{\mu}_{mj}$. The product is to be taken over all possible defect sites, assuming superposition is valid.

We write $\vec{\kappa}$ in terms of the vector set reciprocal to the A_i's and the continuous variables h_1, h_2, and h_3 as $\vec{\kappa} = 2\pi(h_1\vec{B}_1 + h_2\vec{B}_2 + h_3\vec{B}_3)$. Integer values of the continuous variables indicate a reciprocal-lattice point with the Miller indices $h_1 = H$, $h_2 = K$, and $h_3 = L$. Having assumed two possible defect types, AB loops and BA loops, we denote their respective attenuation factors by A_m^{AB} and A_m^{BA}. Then $A_m = A_m^{AB}\cdot A_m^{BA}$. It turns out that Eq. (6) converges rapidly with the distance $\vec{r}_{mj}$ between the mth site and the jth defect site, so that the product may be taken over m instead of j. The factor $\frac{1}{2}\vec{\kappa}\cdot\vec{\mu}_{mj}$ is

$$\tfrac{1}{2}\vec{\kappa}\cdot\vec{\mu}_{mj} = \frac{\pi}{A}\left[\left(\frac{[l_1 + \frac{1}{6}(3 \pm (-1)^n)]\,h_1 + [l_2 + \frac{1}{6}(3 \mp (-1)^n)]\,h_2}{\rho(l_1 l_2 n)}\right)\left(\frac{A_3}{A_1}\right)\mu_r^{\infty}(\rho,\zeta) + \mu_z^{\infty}(\rho,\zeta)\,h_3\right], \tag{7}$$

where the top signs are to be used for AB loops and the bottom signs for BA loops. As long as we are considering $\sin^2\frac{1}{2}\vec{\kappa}\cdot\vec{\mu}_{mj}$ we ask whether there are positions relative to an AB loop for which the magnitude of $\frac{1}{2}\vec{\kappa}\cdot\vec{\mu}_{mj}$ is the same as that for a BA loop? The answer to this is yes, since a B plane is the image of an A plane through the center of a loop which, in turn, is the center of symmetry of the defect. By this argument, it follows that $A_m^{AB} = A_m^{BA}$, and in forming the product in Eq. (6) we may ignore the distinction of signs indicated in Eq. (7) for the two loop types. Since the product in Eq. (6) can be written as a product over $l_1 l_2$ and n, we can drop the exponent $\frac{1}{2}$ and consider only the product for $n \geq 0$.

Here and later in the diffuse scattering we make use of the $\bar{3}$ symmetry to restrict our products to positive values of l_1 and l_2. Given a point at $x\vec{A}_1 + y\vec{A}_2$ there are equivalent points at $-y\vec{A}_1 + (x-y)\vec{A}_2$ and $-(x-y)\vec{A}_1 - x\vec{A}_2$. The coordinate pair $[l_1 + \frac{1}{6}(3 \pm (-1)^n)]$; $[l_2 + \frac{1}{6}(3 \mp (-1)^n)]$ then has equivalent positions $-[l_2 + \frac{1}{6}(3 \mp (-1)^n)]$; $[(l_1 - l_2) \pm \frac{1}{3}(-1)^n]$ and $-[(l_1 - l_2) \pm \frac{1}{3}(-1)^n]$; $-[l_1 + \frac{1}{6}(3 \pm (-1)^n)]$. The values of $\sin\frac{1}{2}\vec{\kappa}\cdot\vec{\mu}_{mj}$ which result we denote as B_i, $i = 1, 2,$ and 3. These same B_i's occur in the diffuse scattering and are given in Table I for the AB loop. For a Bragg reflection we substitute the Miller indices for h_1, h_2, and h_3. Equation (6) can then be written

$$A_m(h_1, h_2, h_3) = \prod_{i=1}^{3} \prod_{l_2=0}^{L(n)} \prod_{l_1=0}^{L(n)} \prod_{n=0}^{n(\epsilon)} [1 - 4P(1-P) B_i^2(l_1, l_2, n, h_1, h_2, h_3)] . \quad (8)$$

The limits on l_1, l_2, and n were chosen to optimize the computer time involved. The limits were chosen so that only atoms whose displacements were larger than a predetermined size were included in the product. The quantity ϵ defines the magnitude of a displacement in units of half the Burgers vector. As ϵ decreases, smaller displacements are taken into account and the number of atoms included in the product becomes larger. The limits $L(n)$ and $n(\epsilon)$ were determined in a computer subroutine and the reader is referred to Appendix A for details.

If a fraction p of the atoms condenses into loops each containing S_L atoms, we write $P = p/S_L$, and express Eq. (8) in terms of p and S_L. The attenuation factor is then a function of p, which is determined from the lattice parameter and S_L the loop size. The loop size then appears explicitly as S_L and implicitly through the B_i's in Eq. (8). Figure 3(a) is a plot of A_m^2 vs $2p$ for loops containing 148.72 atoms for several Bragg reflections with $\epsilon = 0.005$. The reason for the noninteger number of atoms in a loop is clarified in Appendix B. The value obtained for A_m^2 is not strongly dependent upon the value of ϵ if $\epsilon \ll 1$. In Table II we list the values of A_m^2 for loops of this size and for $\epsilon = 0.01$ and $\epsilon = 0.005$, corresponding to the relaxation of 419 070 and 1 192 830 atoms, respectively. The values of A_m^2 in the table differ, at most, by 17.6% so that the values of A_m^2 for $\epsilon = 0.005$ are considered to be sufficiently accurate. Figure 3(a) illustrates the strong dependence of the attenuation on the Miller index L. Within the accuracy of the calculations A_m^2 has almost an exact exponential dependence on p. For this size loop and $\epsilon = 0.005$ the expectation value of $(\vec{\kappa} \cdot \vec{\mu}_m)^2$ or $2M'$ was also computed. Figure 3(b) is a plot of $e^{-2M'}$ vs $2p$. Comparing Figs. 3(a) and 3(b) it is clear that the latter predicts a larger attenuation. The difference between these results is most pronounced when $\langle(\vec{\kappa} \cdot \vec{\mu}_m)^2\rangle$ is large.

If the locus of points in the S_L, p plane for constant values of A_m^2 is plotted, Figs. 4–7 are obtained. Figure 4 shows the locus of such points for the (00·2) reflection for the values of A_m^2 shown on the lines. The other figures are for the (00·4), (10·1), and (10·3) reflections, respectively. These figures were obtained by considering plots similar to Fig. 3(a) for loops containing 7.00, 17.57, 34.95, 58.68, 148.72, 342.77, and 998.12 atoms. The observed exponential dependence of A_m^2 upon p allowed p to be determined accurately for selected values of A_m^2 for each loop size. When the coordinates S_L and p corresponding to these selected values of A_m^2 were plotted logarithmically (Figs. 4–7), it was found that they could be connected by straight lines. The resulting plots allow convenient interpolation for other values of S_L, p, and the attenuation. The observed straight-line relation also warranted extrapolation to loop sizes as large as 4×10^3 atoms. The log-log plotting in these figures demonstrates the almost exponential dependence of A_m^2 upon p, S_L, and the Miller indices. Clearly, large loops are much more effective than small loops in attenuating the Bragg reflections.

These results provide a method of estimating

TABLE I. Various quantities used in the calculation of the attenuation factor and the diffuse scattering. The quantity $R = \frac{1}{4}|A_3|/|A_1| = 0.40824829$.

$$B_1 = \sin\pi\left\{\frac{[[l_1+(3+(-1)^n)/6]h_1+[l_2+(3-(-1)^n)/6]h_2]R\mu^x{}_r(\rho\zeta)}{[[l_1+(3+(-1)^n)/6]^2+[l_2+(3-(-1)^n)/6]^2-[l_1+(3+(-1)^n)/6][l_2+(3-(-1)^n)/6]]^{1/2}}+\frac{\mu^x{}_z(\rho\zeta)h_3}{4}\right\}$$

$$B_2 = \sin\pi\left\{\frac{[-[l_2+(3-(-1)^n)/6]h_1+[(l_1-l_2)+(-1)^n/3]h_2]R\mu^x{}_r(\rho\zeta)}{[[l_2+(3-(-1)^n)/6]^2+[(l_1-l_2)+(-1)^n/3]^2+[l_2+(3-(-1)^n)/6][(l_1-l_2)+(-1)^n/3]]^{1/2}}+\frac{\mu^x{}_z(\rho\zeta)h_3}{4}\right\}$$

$$B_3 = \sin\pi\left\{\frac{-[[(l_1-l_2)+(-1)^n/3]h_1+[l_1+(3+(-1)^n)/6]h_2]R\mu^x{}_r(\rho\zeta)}{[[(l_1-l_2)+(-1)^n/3]^2+[l_1+(3+(-1)^n)/6]^2-[(l_1-l_2)+(-1)^n/3][l_1+(3+(-1)^n)/6]]^{1/2}}+\frac{\mu^x{}_z(\rho\zeta)h_3}{4}\right\}$$

$$C_1 = \cos2\pi\left\{\left[1+\frac{R\mu^x{}_r(\rho0)}{(l_1^2+l_2^2-l_1l_2)^{1/2}}\right](l_1h_1+l_2h_2)\right\}$$

$$C_2 = \cos2\pi\left\{\left[1+\frac{R\mu^x{}_r(\rho0)}{(l_1^2+l_2^2-l_1l_2)^{1/2}}\right](-l_2h_1+(l_1-l_2)h_2)\right\}$$

$$C_3 = \cos2\pi\left\{\left[1+\frac{R\mu^x{}_r(\rho0)}{(l_1^2+l_2^2-l_1l_2)^{1/2}}\right]((l_1-l_2)h_1+l_1h_2)\right\}$$

$$S_1 = \sin\pi\left\{[[l_1+(3+(-1)^n)/6]h_1+[l_2+(3-(-1)^n)/6]h_2]\left[2+\frac{R\mu^x{}_r(\rho\zeta)}{[[l_1+(3+(-1)^n)/6]^2+[l_2+(3-(-1)^n)/6]^2-[l_1+(3+(-1)^n)/6][l_2+(3-(-1)^n)/6]]^{1/2}}\right]+\left[\frac{2(2n+1)+\mu^x{}_z(\rho\zeta)}{4}\right]h_3\right\}$$

$$S_2 = \sin\pi\left\{[-[l_2+(3-(-1)^n)/6]h_1+[(l_1-l_2)+(-1)^n/3]h_2]\left[2+\frac{R\mu^x{}_r(\rho\zeta)}{[[l_2+(3-(-1)^n)/6]^2+[(l_1-l_2)+(-1)^n/3]^2+[l_2+(3-(-1)^n)/6][(l_1-l_2)+(-1)^n/3]]^{1/2}}\right]+\left[\frac{2(2n+1)+\mu^x{}_z(\rho\zeta)}{4}\right]h_3\right\}$$

$$S_3 = \sin\pi\left\{-[[(l_1-l_2)+(-1)^n/3]h_1+[l_1+(3+(-1)^n)/6]h_2]\left[2+\frac{R\mu^x{}_r(\rho\zeta)}{[[(l_1-l_2)+(-1)^n/3]^2+[l_1+(3+(-1)^n)/6]^2-[(l_1-l_2)+(-1)^n/3][l_1+(3+(-1)^n)/6]]^{1/2}}\right]+\left[\frac{2(2n+1)+\mu^x{}_z(\rho\zeta)}{4}\right]h_3\right\}$$

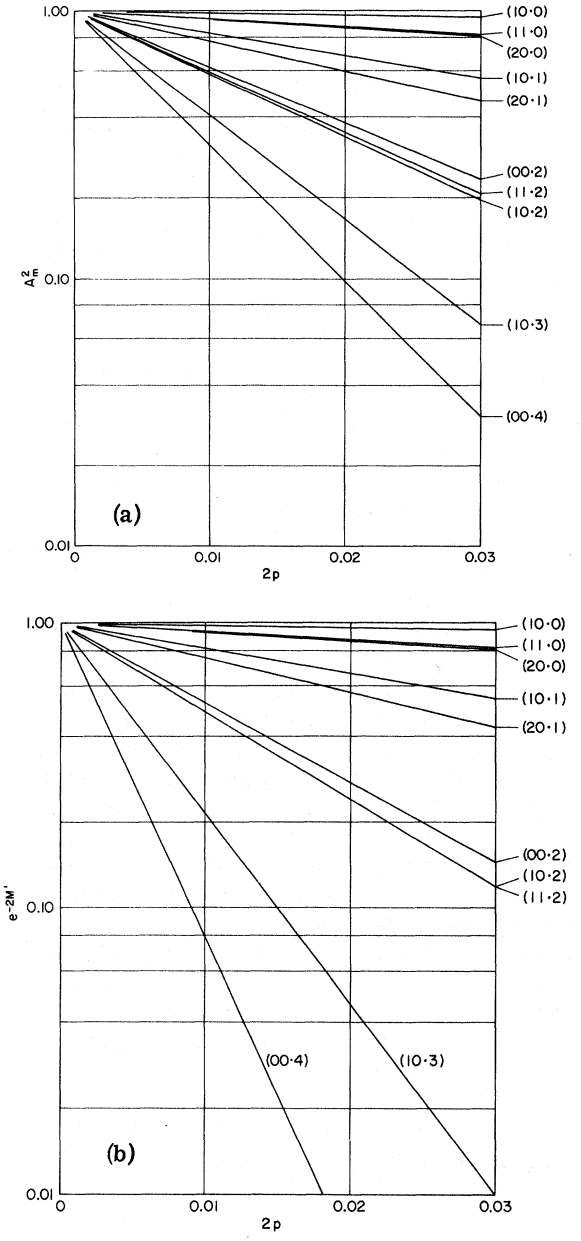

FIG. 3. (a) Plot of attenuation factor A_m^2 vs $2p$ for several Bragg reflections for a loop with $S_L = 148.72$ atoms and $\epsilon = 0.005$. (b) Plot of $e^{-2M'}$ vs $2p$ which predicts too large an attenuation; S_L and ϵ are the same as in (a).

loop size from measurements of lattice parameter and reduction in Bragg intensities. If the experimenter has an estimate of p from the lattice parameter, then Figs. 4–7 provide an estimate of loop size. If the loops are small, the core correction $K(S_L)$ in Eq. (5) and plotted in Fig. 2 may require a new estimate of p and make an iterative procedure for p and S_L necessary. The attenuation depends strongly on the Miller index L, and Figs. 4–7 cover those values of L most useful in practice. This method of determining loop size depends upon the loop displacement field and hence on the elastic properties of the material.

The major effect on the Bragg intensities is due to the attenuation factor. However, there is a small change in the average structure factor of the unit cell because of the occasional occupancy of a C site which is summarized as follows:

$$
\begin{aligned}
(F/f)^2 &= 0\,, && L \neq \text{modulo 2},\ H-K = \text{modulo 3}\\
&= 3(1-p)^2\,, && L \neq \text{modulo 2},\ H-K \neq \text{modulo 3}\\
&= 4(1-2p)^2\,, && L = \text{modulo 2},\ H-K = \text{modulo 3}\\
&= (1+p)^2\,, && L = \text{modulo 2},\ H-K \neq \text{modulo 3}\\
&= 4\,, && L = \text{modulo 4},\ H-K = \text{modulo 3}\\
&= (1-3p)^2\,, && L = \text{modulo 4},\ H-K \neq \text{modulo 3}\\
& && L = 0 \text{ is modulo 4 only}\,. \qquad (9)
\end{aligned}
$$

V. DIFFUSE SCATTERING

We use the following expression for the diffuse scattering:

$$\frac{I_D(\vec{\kappa})}{P(1-P)A_m^2(\vec{\kappa})f^2} = \sum_j^N \left| F_L(\vec{\kappa}) + \sum_m (e^{i\vec{\kappa}\cdot\vec{\mu}_{mj}} - 1)\, e^{i\vec{\kappa}\cdot\vec{r}_{mj}} \right|^2 . \quad (10)$$

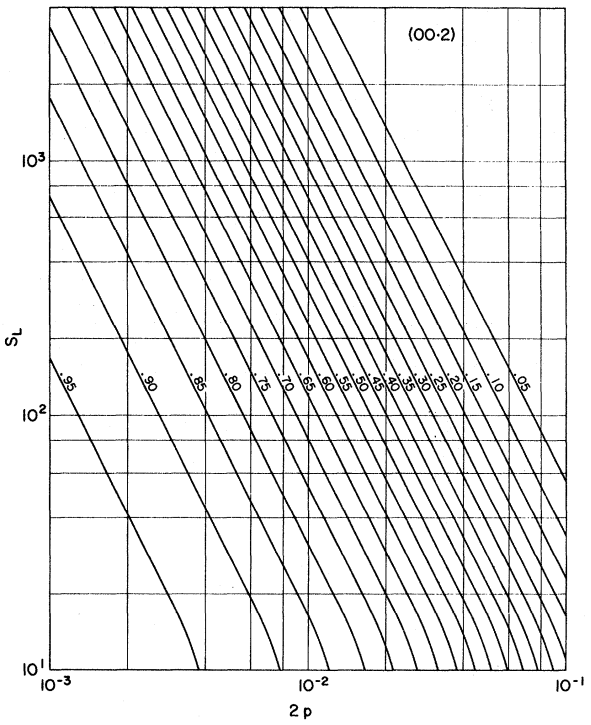

FIG. 4. Loci for selected values of A_m^2 for the (00·2) reflection in S_L, $2p$ plane.

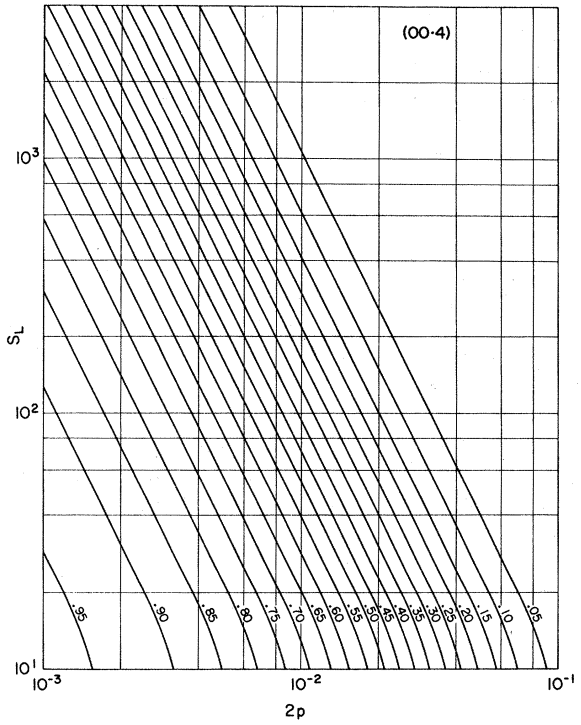

FIG. 5. Loci for selected values of A_m^2 for the (00·4) reflection in S_L, $2p$ plane.

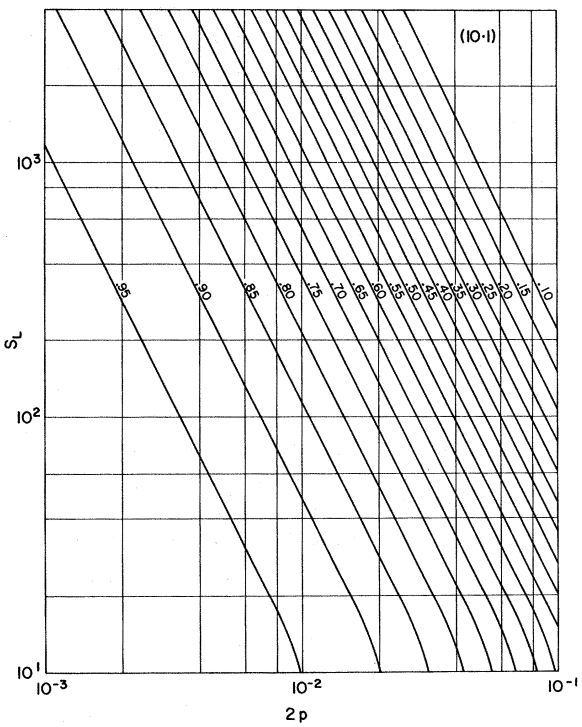

FIG. 6. Loci for selected values of A_m^2 for the (10·1) reflection in S_L, $2p$ plane.

$I_D(\vec{\kappa})$ is the diffuse intensity, f is the atomic scattering factor, $F_L(\vec{\kappa})$ is the geometrical structure factor of the loop, and $\vec{r}_{mj}$ is the vector position of the mth site in our crystal from the jth defect site, in this case the central atom in our loop. The vectors $\vec{r}_{mj}$ should be referred to the *mean (dilated) lattice of the crystal containing defects, and the diffuse intensity is reduced by the attenuation factor given in Eqs.* (6) *and* (8).[33,34] Since AB and BA loops are equally likely, the sum in Eq. (10) extends over all N defect sites. Equation (10) contains several approximations. We have neglected altogether interference effects among different loops. We have included only the interference effects arising from the correlated displacements between two matrix sites m and n due to the presence of a single defect[36] and similarly between the defect (loop) and the matrix displacements. The latter effect is the cross-product term in Eq. (10). Finally, the attenuation factors for loop atoms and matrix atoms were taken to be equal. Not included in Eq. (10) is a slowly varying term equal to $NPS_L \times[1-A_m^2(\vec{\kappa})]f^2$.

The geometrical structure factor of the loop when multiplied by the atomic scattering factor gives the amplitude scattered by the atoms in the loop. In general, a plane of close-packed atoms cannot possess an exactly circular border. We have resorted to the following scheme to ensure our loops are circular. If the center of an atom lies within our circumscribed circle, we consider that this portion in the loop is occupied with a probability represented by the fraction of the atomic volume lying within our circle. Depending upon the l_1, l_2 coordinates of the atom, this fraction $f(l_1, l_2)$ can assume values from $\frac{1}{2}$ to 1. The derivation of this

TABLE II. Values of A_m^2 for $\epsilon=0.010$ and 0.005 corresponding to the relaxation of 419 070 and 1 192 830 atoms, respectively, about a loop of 148.72 atoms, for several reflections ($HK\cdot L$) and several values of p.

	$\epsilon=0.010$				$\epsilon=0.005$			
$2p$	(10·1)	(10·3)	(00·2)	(00·4)	(10·1)	(10·3)	(00·2)	(00·4)
0.001	0.98185	0.91722	0.95386	0.89532	0.98131	0.91404	0.95258	0.89051
0.003	0.94655	0.77165	0.86788	0.71769	0.94498	0.76365	0.86438	0.70617
0.010	0.83267	0.42144	0.62354	0.33097	0.82809	0.40706	0.61519	0.31360
0.030	0.57734	0.07485	0.24244	0.03626	0.56787	0.06745	0.23283	0.03084

fraction is treated in Appendix B. According to our elastic model, the loop itself undergoes a radial shrinkage when it is inserted into the host lattice. The C_i's listed in Table I account for the interference effects of the loop atoms and take into account the radial shrinkage. We then write for the geometrical structure factor of the loop

$$F_L(h_1, h_2) = 1 + \sum_{i=1}^{3} \sum_{l_1 \neq 0} \sum_{l_2 = 0} f(l_1, l_2)\, C_i(l_1, l_2, h_1, h_2)\,. \quad l_1^2 + l_2^2 - l_1 l_2 \leq (c/A_1)^2 \tag{11}$$

The term 1 accounts for the origin atom, and just as in Eq. (8) the symmetry of the loop was used to restrict the sums to positive values of l_1 and l_2. The limits on l_1 and l_2 ensure that the centers of all atoms lie within the circumference of the loop.

Both AB and BA loops possess a center of symmetry, hence the exponentials can be written as

$$-2\sin(\tfrac{1}{2}\vec{\kappa}\cdot\vec{\mu}_{mj})\sin[\vec{\kappa}\cdot(\vec{r}_{mj}+\tfrac{1}{2}\vec{\mu}_{mj})].$$

Half the defect sites in Eq. (10) have $\frac{1}{2}\vec{\kappa}\cdot\vec{\mu}_{mj}$ given by the top set of signs in Eq. (7) and the other half by the bottom set. This is also true for $\vec{\kappa}\cdot\vec{r}_{mj}$, namely,

$$\vec{\kappa}\cdot\vec{r}_{mj} = 2\pi\{[l_1 + \tfrac{1}{6}(3 \pm (-1)^n)]\,h_1 + [l_2 + \tfrac{1}{6}(3 \mp (-1)^n)]\,h_2 + \tfrac{1}{4}(2n+1)\,h_3\}\,. \tag{12}$$

Here as before the top set of signs is to be used for AB loops and the bottom set for BA loops. The only difference in these expressions for $\frac{1}{2}\vec{\kappa}\cdot\vec{\mu}_{mj}$ and $\vec{\kappa}\cdot\vec{r}_{mj}$ for the two loops is the interchange in the roles of l_1 and l_2. Since l_1 and l_2 are to be summed over the same integer set, one can write for the scattering from a BA loop the same expression as that for an AB loop but with h_1 and h_2 interchanged. This is reflected in the expression for the diffuse scattering

$$\frac{I_D(h_1, h_2, h_3)}{(\frac{1}{2}N)P(1-P)A_m^2(h_1, h_2, h_3)\,f^2} = g(h_1, h_2, h_3)$$

$$= \left(F_L(h_1, h_2) - 4\sum_{i=1}^{3}\sum_{l_1=0}^{L(n)}\sum_{l_2=0}^{L(n)}\sum_{n=0}^{n(c)} B_i(l_1, l_2, n, h_1, h_2, h_3)\,S_i(l_1, l_2, n, h_1, h_2, h_3)\right)^2$$

$$+ \left(F_L(h_2, h_1) - 4\sum_{i=1}^{3}\sum_{l_1=0}^{L(n)}\sum_{l_2=0}^{L(n)}\sum_{n=0}^{n(c)} B_i(l_1, l_2, n, h_2, h_1, h_3)\,S_i(l_1, l_2, n, h_2, h_1, h_3)\right)^2 . \tag{13}$$

The S_i's are given in Table I for the AB loop, and the limits on the sums are the same as those used in calculating the attenuation factor, and are discussed there and in Appendix A. The factor 4 in front of the sum consists of the factor of 2 which resulted from expressing the exponentials as circular functions and a factor of 2 to take into account the fact that the sums in Eq. (13) run over only positive values of n. Since the two defects each have $\bar{3}$ symmetry and are related to each other by a $\frac{2}{6}\pi$ rotation, the diffuse scattering has $6/m$ symmetry.

If the loops did not produce atomic displacements in the lattice ($\vec{\mu}_{mj} \equiv 0$), then Eq. (13) would reduce to the square of the geometrical structure factor of the loop. The scattering would then be the two-dimensional reflections of the loop, or HK rods in reciprocal space. However, the total defect is a finite extrinsic fault and we might expect, in analogy to other problems in stacking disorders,[10-17] that rods with $H-K=$ modulo 3 would differ from those with $H-K\neq$ modulo 3. That is, the sums in Eq. (13) which reflect the displacement field produced by the loop may drastically alter the two-dimensional rods expected from only the loops.

In the absence of any strains the C_i's in Table I and Eq. (11) are periodic in the intervals $h_1 = H$ and $h_2 = K$, so that $F^2(h_1, h_2)$ would be strictly periodic. However, the nonuniform strains induced by inserting the loop into the matrix destroy the periodicity in $F^2(h_1, h_2)$. This causes the rods to be displaced outward from the origin, to be reduced in intensity, and to be broadened. The solid curve in Fig. 8 is a plot of $F^2(h_1, 0)$ vs h_1 for a loop with $c/A_1 = 6.5$ or $S_L = 148.72$ atoms. These effects are clearly seen by comparing the peaks at $h_1 = 0$ and $h_1 = 1$. Aside from this perturbation, the scattering from the loop is determined from its shape and size. We may estimate the intensity distribution of the rods from the external form factor of the loop[38] determined by the Fourier transform of a disk having a uniform distribution of scattering per unit area ρ equal to the number of atoms per unit area of the loop. We write

$$F_A(\eta_1, \eta_2) = \rho\int_0^{2\pi}\int_0^{c} e^{i g r\cos\phi}\, r\,dr\,d\phi$$

$$= 2\pi\rho c^2\,[J_1(gc)/(gc)]$$

$$= \pi\rho c^2 \Lambda_1(gc)\,, \tag{14}$$

where $\rho = 2/\sqrt{3}\,A_1^{-2}$ or $\rho\pi c^2 = S_L$. The vector $\vec{g} = 2\pi(\eta_1\vec{B}_1 + \eta_2\vec{B}_2)$ is parallel to the plane of the disc

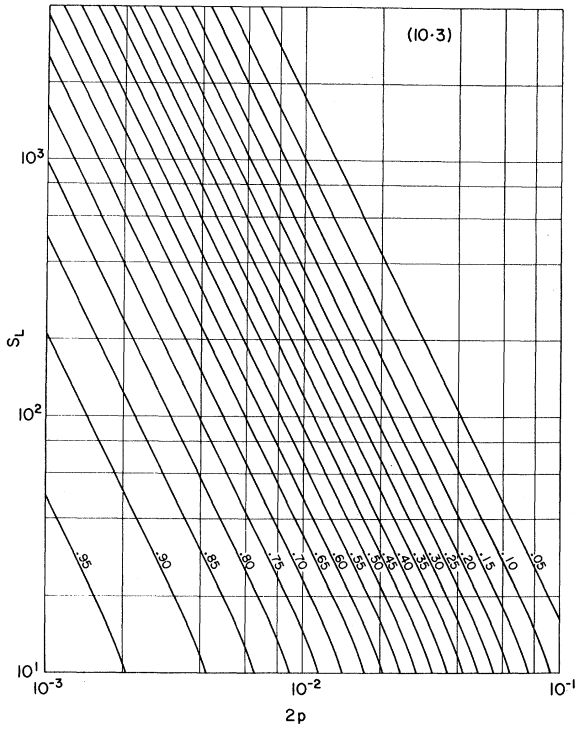

FIG. 7. Loci for selected values of A_m^2 for the (10·3) reflection in S_L, $2p$ plane.

with its origin on the HK rod. The magnitude of $g = 4\pi 3^{-1/2} A_1^{-1}(\eta_1^2 + \eta_2^2 + \eta_1\eta_2)^{1/2}$, and ϕ is the angle between $\vec{g}$ and $\vec{r}$. $J_1(gc)$ is the first-order Bessel function of the first kind and $\Lambda_1(gc)$ is defined and tabulated in Jahnke and Emde.[39] Thus $F_\Lambda^2(\eta_1, \eta_2)$ can be expressed either in terms of c/A or S_L as

$$F_\Lambda^2(\eta_1, \eta_2) = \tfrac{4}{3}\pi^2 (c/A_1)^4 \Lambda_1^2 \times [4\pi 3^{-1/2}(\eta_1^2 + \eta_2^2 + \eta_1\eta_2)^{1/2} cA_1^{-1}]$$

$$= S_L^2 \Lambda_1^2 [2^{3/2}\pi^{1/2} 3^{-1/4}(\eta_1^2 + \eta_2^2 + \eta_1\eta_2)^{1/2} S_L^{1/2}] . \quad (15)$$

The dashed curve in Fig. 8 at $h_1 = 0.5$ is a plot of $F_\Lambda^2(\eta_1, 0)$ for a loop of 148.72 atoms. The η's in Eq. (15) are commensurate with the h's. $F^2(h_1, 0)$ and $F_\Lambda^2(\eta_1, 0)$ are very similar in this region of reciprocal space. The full width at half-maximum (FWHM) of $\Lambda_1^2(x)$ is 3.233. If we define the FWHM in η space as η_w, the size of the loop producing an HK rod is approximately

$$c/A_1 = 0.4456/\eta_w \quad (16a)$$

or

$$S_L = 0.7203/\eta_w^2 . \quad (16b)$$

If Eq. (13) predicts rods in certain regions of reciprocal space whose intensity distribution is proportional to $F^2(h_1, h_2)$, Eqs. (16a) and (16b) may be used to estimate the loop size.

The properties of Eq. (13) are not readily seen by inspection. To gain insight into these properties a computer program was written to evaluate Eq. (13) in the h_1, 0, h_3 and h_1, h_1, h_3 planes of reciprocal space for $0 \le h_1 \le 1.6$ and $0 \le h_3 \le 3.2$ by incrementing the h's in steps of 0.02. Thus, the diffuse scattering was computed for 13 041 points in reciprocal space. A crystallographic contour routine was then used to map contours of isodiffuse scattering or $\mathcal{I}(h_1, h_2, h_3)$. For the case $h_1 = h_2$ both terms in Eq. (13) are identical, so that only one term need be evaluated and its value doubled. Equation (13) represents a formidable amount of computation even for a computer such as the Control Data CDC-6600. The circular-function subroutine, which takes a relatively long time on the computer, was replaced by a scheme suggested by Harris. The scheme substitutes two multiplications and an addition for the circular-function routine. This is discussed in Appendix C. Furthermore, a faster compiler than usual, extended FORTRAN, was used. However, even with these steps, the computation of the diffuse scattering requires long computer times, and, for ϵ fixed, this time increases rapidly with loop size. For $\epsilon = 0.005$ the

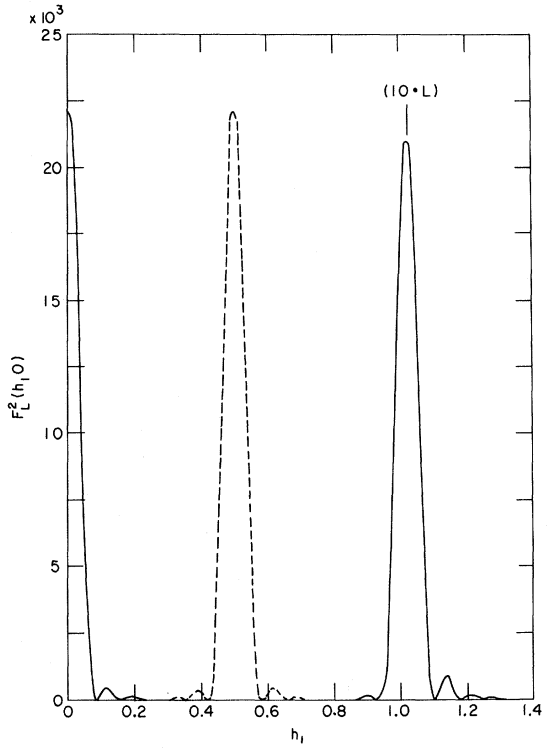

FIG. 8. Plot of $F^2(h_1, 0)$ vs h_1 for $S_L = 148.72$ atoms, solid line. The nonperiodicity is caused by the nonuniform shrinkage of the loop when inserted into the matrix. A plot of $F_\Lambda^2(\eta_1, 0)$, dashed curve, is inserted at $h_1 = \frac{1}{2}$ for comparison.

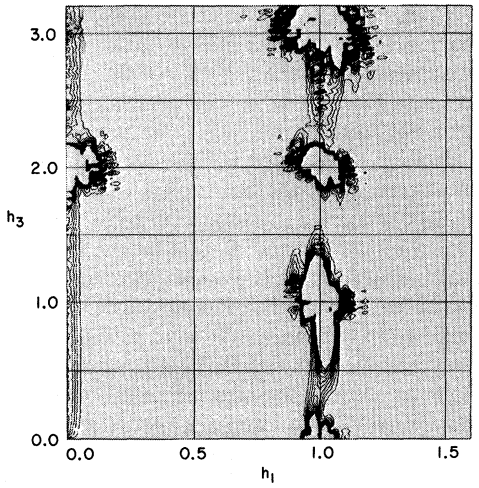

FIG. 9. Isodiffuse intensity contours in h_1, 0, h_3 plane from only the displacements produced by an *AB* loop. Note the $(00 \cdot L)$ rod and the diffuse bridge between $(10 \cdot 0)$ and $(10 \cdot 1)$. There are 10 contours and the interval is 5000.

largest loop which could be economically considered contained 148.72 atoms.

Figures 9–11 illustrate the properties of Eq. (13), $S_L = 148.72$ atoms. In each of these figures there are ten contours and the contour interval is 5000. Figure 9 is the isodiffuse scattering in the h_1, 0, h_3 plane of the reciprocal lattice from the *displacements alone of the AB loop*, or the first term in Eq. (13) with $F^2(h_1, 0)$ set equal to zero. Contours above 50 000 are not plotted because they become too dense. The striking part about this figure is the $(00 \cdot L)$ rod produced by the displacement field alone. This rod is four contours high with a maximum of ~ 20 000. In Fig. 8, the $(00 \cdot L)$ rod from the loop alone has a maximum of 22 118. Along the h_3 axis the loop scattering and displacement scattering are essentially equal. The scattering around the $(10 \cdot 1)$ reflection is extended in the h_3 direction and the $(10 \cdot 0)$ and $(10 \cdot 1)$ reflections are connected by a diffuse streak. Figure 10(a) is the isodiffuse scattering in the h_1, 0, h_3 plane from both the loop and its displacement field for the *AB* loop $[F(h_1, 0) \neq 0]$. The striking part about this figure is the absence of the $(00 \cdot L)$ rod. This can be understood from the fact that the amplitudes scattered by the loop and its displacement field are equal and positive. However, the cross product of the amplitudes scattered by the loop and its displacement field is negative and equal to the sum of the intensities scattered by each. There is also a strong reinforcement of the diffuse scattering bridge between the $(10 \cdot 0)$ and $(10 \cdot 1)$, and likewise between the $(10 \cdot 2)$ and $(10 \cdot 3)$. Figure 10(b) is the isodiffuse scattering in the h_1, 0, h_3 plane from both the loop and its displacement field for the *BA* loop $[F(h_1, 0) \neq 0]$. Again there is no $(00 \cdot L)$ rod, and the strong bridge of diffuse scattering is between $(10 \cdot 1)$ and $(10 \cdot 2)$ in contrast to Fig. 10(a). Figure 11(a) is the isodiffuse scattering in the h_1, 0, h_3 plane from both *AB* and *BA* loops, or from the complete expression in Eq. (13). We see that there is a $(10 \cdot L)$ rod, but its intensity is much larger than that expected from the loops only. There is also a characteristic hook in the rod at the $(10 \cdot 0)$ reflection. Figure 11(b) is the isodiffuse scattering in the h_1, h_1, h_3 plane from both *AB* and *BA* loops. There are no rods, and the diffuse scattering is localized around allowed Bragg

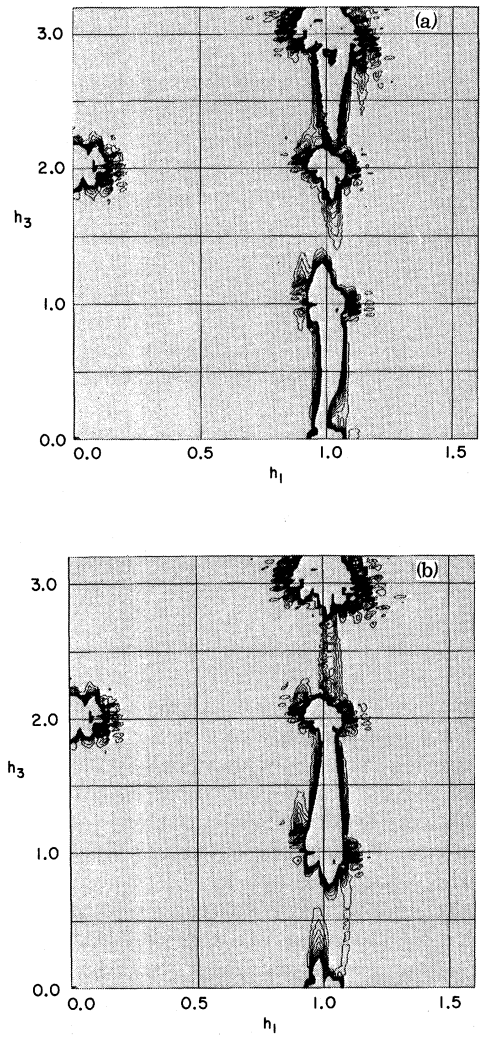

FIG. 10. (a) Isodiffuse intensity contours in h_1, 0, h_3 plane from *AB* loops. Note the absence of the $(00 \cdot L)$ rod and the strengthening of the diffuse bridge between $(10 \cdot 0)$ and $(10 \cdot 1)$. (b) Same as (a) but for *BA* loops. Note absence of an $(00 \cdot L)$ rod and diffuse bridge between $(10 \cdot 1)$ and $(10 \cdot 2)$. Contours are the same as in Fig. 9.

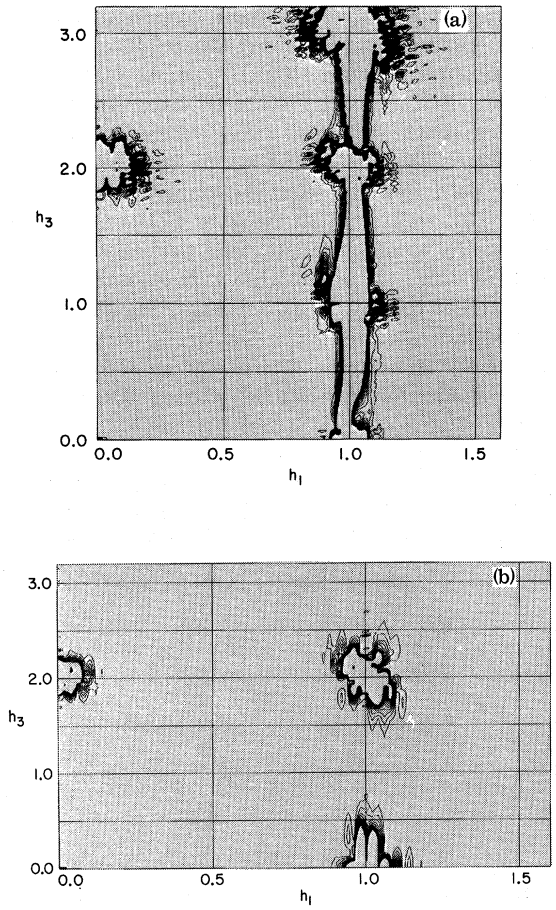

FIG. 11. (a) Isodiffuse intensity contours in the h_1, 0, h_3 plane for both AB and BA loops. Note absence of the $(00 \cdot L)$ rod and the presence of the $(10 \cdot L)$ rod. (b) Same as (a) but in the h_1, h_1, h_3 plane. Note absence of rods and the diffuse scattering localized in the vicinity of the Bragg reflections. The contours are the same as in Fig. 9.

reflections. Finally in Fig. 12 we have replotted Fig. 11 but with a change in contour levels; here there are ten contours with a contour interval of 50 000. Figure 12 indicates more clearly the shape of the intense diffuse scattering close to the Bragg reflections. It should be noted that the diffuse scattering around the $(00 \cdot 2)$, $(10 \cdot 1)$, $(10 \cdot 2)$, and $(10 \cdot 3)$ is significantly displaced from integer values of h_3 to values that are somewhat larger. The center of the diffuse maximum about the $(00 \cdot 2)$ is displaced such that $\Delta L/L \sim 0.014$. Figures 9–12 exhibit some spurious ripples and islands of intensity which are attributable to the termination of the series in Eq. (13) representing the diffuse scattering.[40]

Our defect which is a finite extrinsic fault reveals its disturbance of the hcp stacking sequence most clearly in those regions of reciprocal space where $H - K \neq$ modulo 3. In those regions of reciprocal space where $H - K =$ modulo 3 there is a strong diffuse scattering in the vicinity of the Bragg peaks which is more sensitive to the symmetry of the displacement field of the loop than to the disturbance the loop introduces in the stacking sequence. Note in Figure 12(b) the similarity of the isodiffuse scattering contours around $(11 \cdot 0)$ to the contours of the r component of the displacement field in Fig. 1(a). In this case the diffraction vector is essentially parallel to the r components of the displacement field and perpendicular to the z components. Likewise the isodiffuse scattering contours around $(00 \cdot 2)$ are similar to the contours of the z component of the displacement field in Fig. 1(b), since the diffraction vector is essentially parallel to the z components of the displacement field and normal to the r components.

It is natural to ask whether anything in the diffuse scattering characterizes the size of the loops present. We have noted that the amplitude of the $(00 \cdot L)$ rod scattered from the loop alone is can-

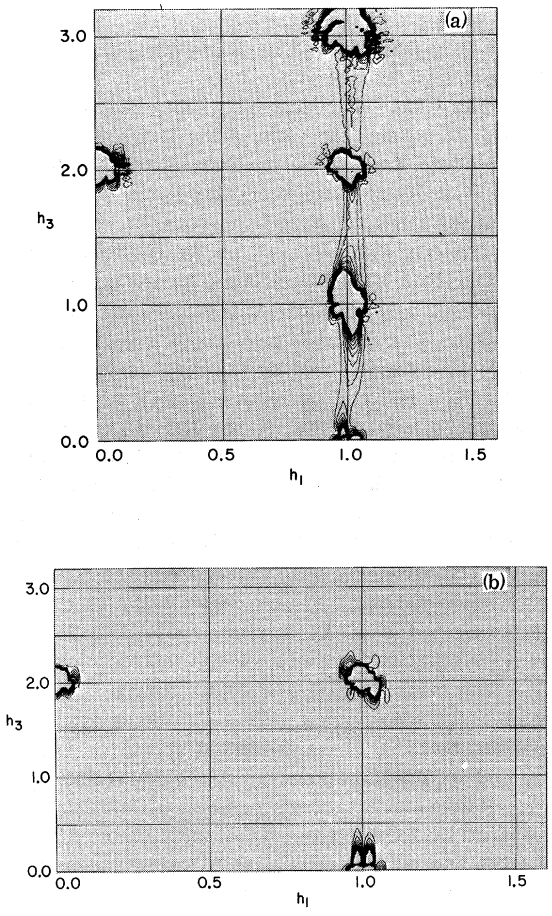

FIG. 12. Same as Fig. 11 but here there are 10 contours with a contour interval of 50 000.

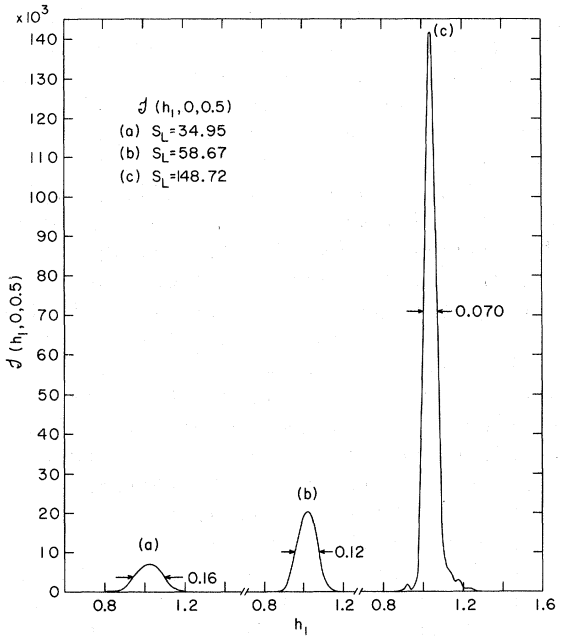

FIG. 13. Plot of $\mathcal{I}(h_1, 0, \frac{1}{2})$ vs h_1 for loops with values of $S_L = 34.95$, 58.67, and 148.72, respectively.

celled by the amplitude scattered from the displacements. Similarly, we have noted that along the $(10 \cdot L)$ rod the displacement scattering may tend to either reinforce or cancel the amplitude scattered by the loop. Figure 13 is a plot of $\mathcal{I}(h_1, 0, \frac{1}{2})$ vs h_1 for loops with c/A_1 equal to 3.146, 4.106, and 6.500, or with values of S_L equal to 34.95, 58.67, and 148.72, respectively, for curves (a), (b), and (c). The half-widths η_w are indicated for each curve. If similar plots are made in the vicinity of $h_3 = \frac{1}{2}$ we find that although the intensity may vary, these half-widths are reasonably constant. If we insert the values of η_w indicated in Fig. 13 into Eqs. (16a) and (16b), we find values of c/A_1 equal to 2.8, 3.7, and 6.4, and values of S_L equal to 28.1, 50.0, and 147.0, respectively. These values compare well with the values used in the calculations. These results suggest that a measurement of the FWHM of the $(10 \cdot L)$ rod midway between $(10 \cdot 0)$ and $(10 \cdot 1)$ can be used to estimate the size of loops present in the crystal.

VI. DISCUSSION

To compare our results with a hcp material in which interstitial dislocation loops are known to exist, we have chosen neutron-irradiated BeO. An extensive literature exists[41] on neutron-irradiated BeO and Wilks[42] has recently reviewed the subject. BeO has the wurtzite structure, with almost the ideal A_3/A_1 ratio $(\frac{8}{3})^{1/2}$ $(A_3/A_1 = 1.623)$ and is essentially elastically isotropic with a Poisson's ratio of 0.249.[43] Rau[6] has positively identified basal-plane loops in BeO irradiated with neutrons to 5.3×10^{20} n/cm^2 $(E \geq 1$ MeV) at 1000 °C. At lower irradiation temperatures ~ 100 °C and for exposures less than ~ 10^{20} n/cm^2 resolvable dot clusters are seen along with a "textured" background. For exposures over 2×10^{20} n/cm^2 a very large number of dot clusters, estimated to be approximately 50–100 Å in diameter, are seen which are interpreted as small interstitial loops oriented on the basal planes.[5] Clearly, interstitial basal-plane loops that can be seen in the electron microscope are produced in BeO under certain conditions, and there is reason to believe that under other conditions loops are also produced that are too small to be clearly identified as loops in the electron microscope.

Figure 14 is a reproduction of a sequence of x-ray diffractometer traces taken by Rau and Chase of irradiated BeO samples.[5] These traces were taken on samples of polycrystalline BeO rods formed by extrusion and sintering, and after irradiation crushed to 10-μ particle size. Thus it is reasonable to assume that these samples are free of intergranular strain.[44] The rods were irradiated in the Engineering Test reactor in Idaho at ~ 100 °C to exposures from 0.5 to 11.7×10^{20} n/cm^2 $(E \geq 1$ MeV). These traces illustrate graphically a number of the effects predicted for the x-ray pattern of a hcp material containing interstitial basal-plane loops. The $(10 \cdot 0)$ reflection remains essentially unchanged in both position and intensity with increasing exposure. Since basal-plane loops pro-

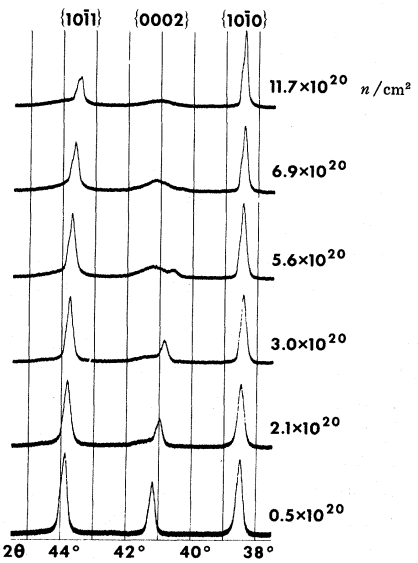

FIG. 14. Diffractometer traces of neutron-irradiated BeO powders $(E \geq 1$ MeV). Effects of irradiation are more pronounced for large values of the Miller index L. The effects seen are explained by interstitial basal-plane loops which increase in number and size with exposure.

duce no change in the $\vec{A}_1$ lattice parameter, Eq. (4a), this is exactly what is expected for a reflection with a Miller index $L = 0$. Furthermore, referring to Fig. 3(a), the attenuation factor $A_m^2(10 \cdot 0)$ is nearly 1 for any reasonable value of p. This is true for all size loops. The $(00 \cdot 2)$ reflection shifts progressively to smaller angle, $\vec{A}_3$ expanding, and decreases in intensity with increasing exposure. Since basal-plane loops do produce a change in the $\vec{A}_3$ parameter Eq. (4b), this is exactly as expected. The attenuation factor A_m^2 $(00 \cdot 2)$ in Fig. 4 decreases with increasing values of p or S_L. Hence the decrease in $(00 \cdot 2)$ intensity is to be expected if either the number of loops increases, or their size increases, or if a combination of these effects takes place with increasing exposure. The $(10 \cdot 1)$ reflection shifts to lower angle and decreases in intensity with increasing exposure, and behaves in a fashion intermediate between $(10 \cdot 0)$ and $(00 \cdot 2)$. It should be noted that the $(00 \cdot 2)$ and $(10 \cdot 1)$ reflections remain sharp, but as the exposure increases there is an increase in the diffuse scattering on the high-angle side of the reflections. The center of the computed diffuse maximum in Fig. 11 is displaced to the high-angle side of the $(00 \cdot 2)$ such that $\Delta L/L \sim 0.014$. This corresponds to a separation in scattering angle of about $0.6°$ between the $(00 \cdot 2)$ Bragg reflection and its diffuse maximum, which is approximately that observed in Fig. 14. Note that the isodiffuse scattering contours in Fig. 11 are such as to produce a diffuse scattering on the high-angle side of the $(10 \cdot 1)$, which is also observed in Fig. 14. Sometime after the disappearance of the $(00 \cdot 2)$ reflection the diffuse scattering also decreases with increased exposure. This would seem to confirm the argument for the presence of an attenuation factor in the expression for the diffuse scattering.[32-34] All of the effects seen in Fig. 14 are in qualitative agreement with x-ray effects we have predicted for interstitial basal-plane loops.

The traces in Fig. 14 were taken on samples made by applying a thin layer of BeO powder mixed with grease to a microscope slide.[45] This is a good procedure for lattice parameter studies on a material such as BeO which is transparent to x rays.[46] Unfortunately, for intensity measurements, this technique can introduce errors. It is unlikely that the same amount of material was bathed by the x-ray beam in each trace, and it is also unlikely that the degree of preferred orientation is the same for each trace in Fig. 14. Unirradiated BeO gave a diffraction pattern almost identical with the trace of the 0.5×10^{20}-n/cm^2 sample.[5] Table III lists those parameters necessary for determining p and S_L from lattice parameter and intensity measurements.[45] Taking the peak areas of the 0.5×10^{20}-n/cm^2 sample to be the same as an unirradiated sample,

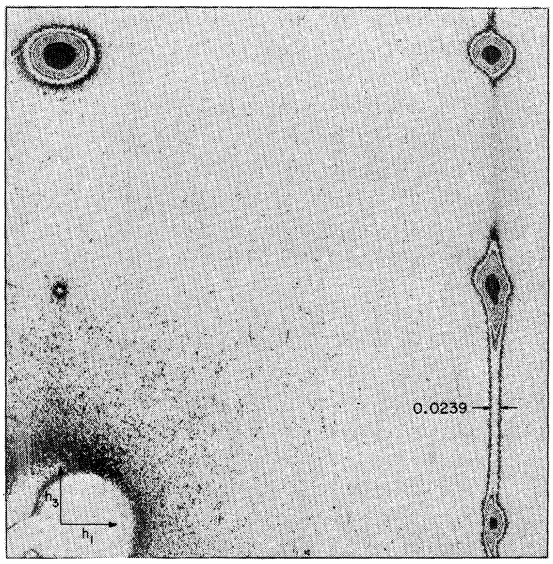

FIG. 15. Isodensitracing of a precession photograph of the h_1, 0, h_3 plane in the reciprocal space of a neutron-irradiated BeO crystal. The exposure is 2.1×10^{20} n/cm^2 ($E \geq 1$ MeV). Compare the figure to Figs. 11(a) and 12(a). From the width of the $(10 \cdot L)$ rod indicated, the loops contain ~1260 BeO molecules. The weakness of the rod between $(10 \cdot 1)$ and $(10 \cdot 2)$ is due to the destructive interference between Be and O.

the appropriate attenuation factors for the other exposures may be approximately calculated. It is worth noting that the peak areas of the $(10 \cdot 0)$, $(00 \cdot 2)$, and $(10 \cdot 1)$ in Table III for the 0.5×10^{20}-n/cm^2 trace are in the proportion 1.00/0.636/1.00, whereas the products of the square of the structure factor and multiplicity are in the proportion 1.00/0.686/1.735. Presumably, this discrepancy is due to preferred orientation. Rows 8, 9, and 10 in Table III list the zero-order values $2p_0$ and S_L^0, determined by the methods outlined in Sec. IV. The next three rows are the first-order values [first iteration values with $K(S_L) = 0.75$] of $2p_1$ and S_L^1. The numbers for S_L are BeO pairs. We notice that the values of S_L determined from the attenuation of the $(00 \cdot 2)$ and $(10 \cdot 1)$ differ by at least a factor of 4, and that although there is a trend of loop growth with exposure, the main effect is due simply to the increased numbers of loops. A loop consisting of 620 BeO molecules is ~70 Å in diameter, while a loop consisting of 180 BeO molecules is ~40 Å in diameter. Rau estimates the loops in these specimens are 70–100 Å in diameter.[5]

A more severe test for the predictions of the scattering effects from interstitial basal-plane loops is the diffuse scattering. We have already seen that the diffuse scattering in the powder patterns of Fig. 14 is consistent with our computed isodiffuse contours. Figure 15 is a view of the

diffuse scattering[47] in the h_1, 0, h_3 plane of the reciprocal lattice of a BeO crystal neutron irradiated to $2.1\times10^{20} n/cm^2 (E \geq 1\,MeV)$ at a temperature ~100°C in the HIFAR reactor at Lucas Heights.[48] The film from which this figure was made was exposed with monochromatic copper K_α radiation. A Technical Operations model No. 505 isodensitracer was used to record the density of the film. The h_3 and h_1 axes are indicated in the figure. Along the h_3 axis we see the (00 · 4) Bragg peak from the half-wavelength passed by the monochromator and then the (00 · 2) reflection and diffuse scattering which is approximately elliptical in shape. The major axis is perpendicular to the h_3 axis, and the ratio of the major to minor axis is ~1.33. In Fig. 11 of the computed scattering this ratio is ~1.28 (maximum contour). The intersection of the major and minor axes of the diffuse scattering around the (00 · 2) in Fig. 15 is displaced from the Bragg position by $\Delta L/L \sim 0.0135$. Integer values of L in the figure are multiples of the distance from the origin to the half-wavelength peak. The rod of diffuse scattering joining the (10 · $\bar{1}$) and (10 · 0) has a very characteristic S shape which is mirrored through the (10 · 0) to the (10 · 1). This S shape is clearly reproduced in the isodiffuse computer contours in Figs. 11(a) and 12(a). Computations for smaller loops show that the curvature of the S shape is greater for smaller loops. The intense diffuse scattering in the vicinity of the (10 · 1) reflection in Fig. 15 has the shape of a "left footprint." The sole of the foot steps over the value $L = 1$ more than the heel lies behind it. This left footprint is clearly seen in computer contours of Fig. 12(a). The intense diffuse scattering in the neighborhood of the (10 · 2) reflection in Fig. 15 has the shape of a "tear drop" with the tail directed toward (10 · 1). The centroid of the tear drop lies at a value of $h_3 > 2$. Again, compare this with Fig. 12(a).

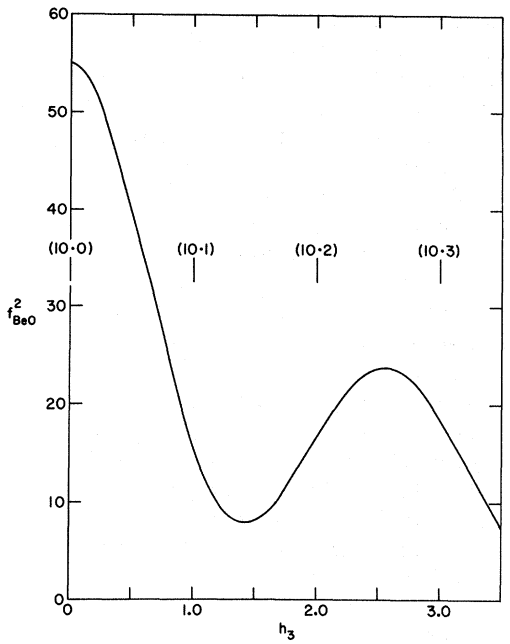

FIG. 16. Plot of f^2_{BeO} vs h_3. The small values for $1.0 \leq h_3 \leq 2.0$ explain the weakness of the (10 · L) rod between (10 · 1) and (10 · 2) in Fig. 15.

In a wurtzite structure such as BeO each close-packed layer can be thought of as a double layer made up of beryllium-oxygen pairs. The pair separation is μA_3 with $\mu = 0.365$.[49] Rau[6] clearly illustrates the interstitial double-layer loop of BeO pairs in the C position of $ABAB\cdots$ double layers. The interference effects of the BeO pair in BeO can be approximately accounted for by replacing f^2 in Eq. (13) by f^2_{BeO}, where $f^2_{BeO} = f^2_{Be} + f^2_O + 2f_{Be}f_O \times \cos 2\pi\mu h_3$. This function is plotted in Fig. 16. The small values of f^2_{BeO} for $1.0 \leq h_3 \leq 2.0$ explain the weakness of the (10 · L) rod between the (10 · 1) and (10 · 2) reflections in Fig. 15. In addition,

TABLE III. Table for determining loop sizes in neutron-irradiated BeO from the x-ray traces in Fig. 13. $K(S_L)$ was taken to be 0.75.

Exposure (n/cm^2)	0.5×10^{20}	2.1×10^{20}	3.0×10^{20}	5.6×10^{20}	6.9×10^{20}	11.7×10^{20}
$\Delta A_3/A_3$	0.001 256	0.005 802	0.007 950	0.016 242	0.022 158	0.035 864
I(10 · 0) in.^{2}	9.24	8.17	7.69	8.58	6.96	6.87
I(00 · 2) in.^{2}	5.88	2.47	2.00	0.43	···	···
I(10 · 1) in.^{2}	9.26	7.90	7.39	6.38	4.30	2.46
A^2_m(00 · 2)	···	0.420	0.340	0.073	···	···
A^2_m(10 · 1)	···	0.853	0.798	0.689	0.464	0.266
$2p_0$	0.0025	0.0116	0.0159	0.0325	0.0443	0.0717
S^0_L(00 · 2)	···	360	300	420	···	···
S^0_L(10 · 1)	···	81	86	57	130	147
$2p_1$	0.0019	0.0087	0.0119	0.0244	0.0332	0.0538
S^1_L(00 · 2)	···	630	530	710	···	···
S^1_L(10 · 1)	···	145	155	102	230	265

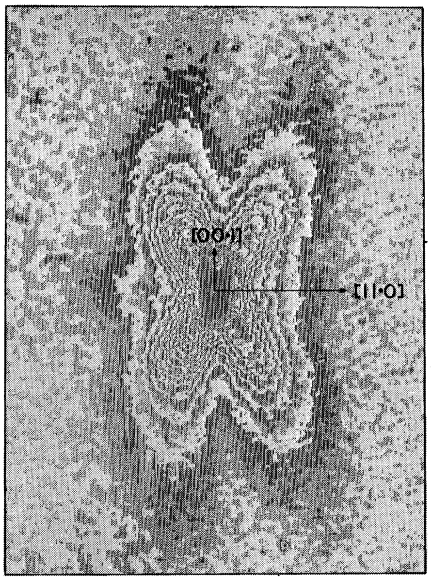

FIG. 17. Isodensitracing of an oscillation photograph of a neutron-irradiated BeO crystal. The exposure is 2.0×10^{20} n/cm^2 ($E\geq1$ MeV). The angle of oscillation is 2.5° on both sides of the (11·0) and the axis of rotation is (00·1). Compare the figure to Figs. 11(b) and 12(b).

the attenuation factor in Eq. (13) is operating to decrease the intensity of the rod as h_3 increases. The full width of the rod at half-maximum at $h_3=\frac{1}{2}$ indicated in Fig. 15 was determined by a densitometer scan parallel to h_1 (the full width at 0.699 maximum of the densitometer scan). Using this value for η_w in Eqs. 16(a) and 16(b) we estimate $c/A=18.6$ or $S_L=1260$ BeO pairs. Thus the loops in the crystal are ~100 Å in diameter. We are aware of other single-crystal studies[50,51] which substantiate Millar's observations. However, Belbéoch *et al.*[52,53] show photographs which illuminate other parts of the reciprocal space of neutron-irradiated BeO. In their[52] Figs. 3 and 4 we observe that as the (10·L) rod becomes broader (smaller loops) its S shape becomes more curved. In their Fig. 3 one observes the diffuse scattering around the (11·0) position of a crystal irradiated to 2×10^{20} n/cm^2 (fast) which appears as a "cross." This is more clear in their[53] Fig. 9 which is an oscillation diagram through the (11·0) reflection. Figure 17 is an isodensitracing of the diffuse scattering in the vicinity of the (11·0) reflection of a BeO crystal irradiated to 2.0×10^{20} n/cm^2($E\geq1$ MeV) at a temperature ~100 °C in the French Triton reactor. The film from which the tracing was made is an oscillation photograph exposed with monochromatic Cu K_α radiation.[54] The "cross" is clearly seen in the isodiffuse contours of our Figs. 11(b) and 12(b). The diffuse scattering at (11·0) reflects the symmetry of the r component of the loop displacement field of Fig. 1(a).

We mention the possibility of explaining some of the puzzling results observed by Walker *et al.*[44] They observed that in samples with the same exposure, the weakening of the Bragg reflections increased as the temperature of the irradiation was raised, although the $\vec{A}_3$ axis expansion decreased. Further, in isochronal anneals of a sample irradiated at ~100 °C they observed that the recovery in the $\vec{A}_3$ axis expansion preceded the recovery in the weakening of the Bragg reflections and diffuse scattering. We have seen in Eq. (5) that the fraction of atoms present in loops p, apart from the weak dependence on loop size, is determined by the expansion of the $\vec{A}_3$ axis. We have seen in Figs. 4–7 that p and the loop size are independent parameters. Even though p may be reduced by choosing loops of appropriate size, the attenuation factor may be made as small as desired. Concomitant with a small value of A_m^2 is a large diffuse scattering.[34] This leads one to conclude that for high exposure temperatures the fraction of atoms in loops is small, but the loops that are present are large.[6] During annealing, a large fraction of the atoms in loops may disappear, but those remaining cluster into larger loops.

In summary, we have used an elastic-continuum model to describe the displacement field produced by a dislocation loop. Although this approach cannot be quantitatively correct for all the displacements, it is thought that it is qualitatively a reasonable approach. For large loops the dimensions of the defect are such that the continuum model becomes quantitative for displacements other than those associated with the dislocation core of the loop. We have discussed the diffraction effects expected to result from interstitial basal-plane loops in a hcp structure, and compared these effects to those observed in neutron-irradiated BeO. BeO is a material in which such defects have been observed in the electron microscope. The predictions of our model are confirmed in every aspect, and we have used them to estimate values of the concentrations and sizes of the loops in neutron-irradiated BeO as well.

ACKNOWLEDGMENTS

The authors wish to acknowledge the valuable assistance of Lydia Bargiuk whose computer programming made this problem tractable. We also wish to acknowledge the valuable assistance of Patricia Moll for her assistance in running and refining the program. We wish to thank A. D. S. Harris for his valuable suggestion which reduced the computer time. We also wish to express our appreciation to Peter Kemmey for providing the subroutine mentioned in Appendix A. We are indebted to Robert C. Rau for the use of his scans in Fig. 14 and data

Table III, and for his discussions of irradiated BeO BeO. We wish also to thank John J. Millar for the use of his excellent precession photograph of the diffuse scattering shown in Fig. 15, and Bella Belbéoch for her oscillation photograph shown in Fig. 17. Finally, we express our gratitude to Leonard Galanter for assistance in the densitometry of Millar's film.

APPENDIX A: LIMITS FOR SUMS AND PRODUCTS

The smallest displacement, in units of half the Burgers vector, retained in the calculations is ϵ. Thus, ϵ generates a locus of points outside of which the magnitude of the displacements is less than ϵ, and these displacements are not considered. We have shown[22] that for large distances from the loop the displacements given by Eqs. (1a) and (1b) approach those for an "infinitesimal loop."[20] The displacements for an infinitesimal loop in terms of $\frac{1}{2}\vec{b}$ are given by Eqs. (8a) and (8b) of Ref. 22 as

$$\mu_r^{\infty}(R_0,\theta) = -\frac{c^2}{4R_0^2}\left(\frac{1-2\sigma}{1-\sigma}\right)\left(1-\frac{3\cos^2\theta}{1-2\sigma}\right)\sin\theta\ , \tag{A1a}$$

$$\mu_z^{\infty}(R_0,\theta) = \frac{c^2}{4R_0^2}\left(\frac{1-2\sigma}{1-\sigma}\right)\left(1+\frac{3\cos^2\theta}{1-2\sigma}\right)\cos\theta\ . \tag{A1b}$$

R_0 and θ are the distance and angle in a cylindrical coordinate system centered on the loop to the point in question, and $R_0 = c(\rho^2+\zeta^2)^{1/2}$, $\cos\theta = \zeta(\rho^2+\zeta^2)^{-1/2}$, and $\sin\theta = \rho(\rho^2+\zeta^2)^{-1/2}$. For small values of ϵ the displacements given by Eqs. (1a), (1b), (A1a), and (A1b) are similar (see, for instance, Figs. 2 and 3 of Ref. 22). Hence we used the locus of points generated by the displacements of Eqs. (A1a) and (A1b) which satisfy the condition

$$\epsilon = \{[\mu_r^{\infty}(R_0,\theta)]^2 + [\mu_z^{\infty}(R_0,\theta)]^2\}^{1/2}\ . \tag{A2}$$

The general shape of this locus is seen in Fig. 2 of Ref. 8. In terms of ρ and ζ, Eq. (A2) becomes

$$\epsilon = \frac{1}{4}\left(\frac{1-2\sigma}{1-\sigma}\right)\left(1+\frac{9\zeta^4}{(1-2\sigma)^2(\rho^2+\zeta^2)}+\frac{6\zeta^2(\zeta^2-\rho^2)}{(1-2\sigma)(\rho^2+\zeta^2)}\right)^{1/2}\frac{1}{(\rho^2+\zeta^2)}\ . \tag{A3}$$

A further simplification was made, namely, that the limits on l_1 and l_2 [called $L(n)$] when $\zeta = \frac{1}{4}(2n+1)\times(A_3/c)$ are determined with sufficient accuracy for our purposes by setting $\rho = L(n)(A_1/c)$. Equation (A3) becomes

$$\epsilon = \frac{1}{4}\left(\frac{1-2\sigma}{1-\sigma}\right)\left(\frac{c}{A_1}\right)^2 R^{-2}U^{-1}(2n+1)^{-2} \times[1+9(1-2\sigma)^{-2}U^{-2}+6(1-2\sigma)^{-1}VU^{-2}]\ . \tag{A4}$$

R is defined in Table I, $U = 1+[L(n)/(2n+1)R]^2$. and $V = 1-[L(n)/(2n+1)R]^2$.

A subroutine in the computer program, supplied by Kemmey, determined the integer value of $L(n)$ which most nearly satisfied Eq. (A4) for each n. As n increases there is a value $n(\epsilon)$ for which no value of $L(n) > 0$ satisfies Eq. (A4) and this value is the limit on n in Eqs. (8) and (13).

APPENDIX B: NUMBER OF ATOMS IN A LOOP

We define the distance to an atom center $\rho = (A_1/c)(l_1^2+l_2^2-l_1l_2)^{1/2}$. When $\rho = 1$, the atom center lies on the loop circumference, and for $\rho(l_1,l_2) < 1$ the atom center lies within the circumference. Thus the limits on l_1 and l_2 in Eq. (11) are determined by the condition

$$l_1^2+l_2^2-l_1l_2 \le (c/A_1)^2\ . \tag{B1}$$

In the same units as ρ the radius of an atom is $r = A_1/2c$. If the coordinate pair l_1 and l_2 is such that $\rho \le 1-A_1/2c$ or if

$$l_1^2+l_2^2-l_1l_2 \le (c/A_1-\tfrac{1}{2})^2\ , \tag{B2}$$

the atom lies completely within the loop and $f(l_1, l_2) = 1$. If the atom center lies between the conditions given by Eqs. (B1) and (B2), we assume that the site is occupied with a probability equal to the volume fraction of the atom within the circumference of the loop. We approximate the volume of the atom within the loop as the spherical segment of one base whose height is $h = (1+\rho^2-r^2)/2\rho$ and whose semibase is $S = \{r^2-[(1-\rho^2-r^2)/2\rho]^2\}^{1/2}$. The volume of the segment is $\frac{1}{6}\pi h(3S^2+h^2)$. Thus we have

$$f(l_1,l_2) = \frac{1}{4}\left[2-\left(\frac{1-\rho^2-r^2}{2\rho r}\right)\right]\left[1+\left(\frac{1-\rho^2-r^2}{2\rho r}\right)\right]^2\ , \tag{B3}$$

with $\rho = (A_1/c)(l_1^2+l_2^2-l_1l_2)^{1/2}$ and $r = A_1/2c$. A subroutine was incorporated in the program which tested the coordinate pairs according to the condition indicated in Eq. (B2), and if the condition was met, $f(l_1, l_2)$ was set equal to 1. If this test failed but that of Eq. (B1) was met, Eq. (B3) was used to compute $f(l_1, l_2)$.

APPENDIX C: METHOD OF EVALUATING CIRCULAR FUNCTIONS

The computation of the diffuse scattering in Eq. (13) requires evaluation of the B_i's and S_i's of Table I. The computation time can be reduced considerably if the routine of computing the sine function for each new value of the argument can be eliminated. Consider that $h_2 = 0$, and h_1 and h_3 in the

argument are incremented by increments of Δh_1 and Δh_3, respectively. Consider the evaluation of the circular functions

$$S_{m,n} = \sin(\alpha m \Delta h_1 + \beta n \Delta h_3) ,$$
$$C_{m,n} = \cos(\alpha m \Delta h_1 + \beta n \Delta h_3) , \quad \text{(C1)}$$

where m and n are integers. If we use the addition theorem for the circular function, we can write

$$S_{m,n} = S_{m-1,n} C_{10} + C_{m-1,n} S_{10} = S_{m,n-1} C_{01} + C_{m,n-1} S_{01} , \quad \text{(C2)}$$
$$C_{m,n} = C_{m-1,n} C_{10} - S_{m-1,n} S_{10} = C_{m,n-1} C_{01} + S_{m,n-1} S_{01} ,$$

where

$$S_{10} = \sin\alpha\Delta h_1 , \quad S_{01} = \sin\beta\Delta h_3 ,$$
$$C_{10} = \cos\alpha\Delta h_1 , \quad C_{01} = \cos\beta\Delta h_3 , \quad \text{(C3)}$$

and

$$S_{00} = 0 , \quad C_{00} = 1 .$$

Equations (C2) are valid when the subscripts are equal to, or greater than, zero. Thus the sine of any point in the first quadrant of the h_1 h_3 plane can be generated after the four circular functions in Eq. (C3) have been computed. This scheme proved much faster with essentially no loss of accuracy.

---

*Work supported by the U. S. Atomic Energy Commission.

[1]J. B. Gibson, A. N. Goland, M. Milgram, and G. H. Vineyard, Phys. Rev. 120, 1229 (1960).

[2]R. A. Johnson, Phys. Rev. 134, A1329 (1964); 145, 423 (1966).

[3]See, e.g., M. Wilkens, in *Vacancies and Interstitials in Metals*, edited by A. Seeger *et al.* (North-Holland, Amsterdam, 1970), pp. 485–529; M. Rühle, *Radiation Damage in Reactor Materials* (International Atomic Energy Agency, Vienna, 1969), Vol. I, pp. 113–156.

[4]R. C. Rau, J. Nucl. Mater. 20, 141 (1966).

[5]R. C. Rau and G. A. Chase, Phys. Status Solidi 19, 645 (1967).

[6]R. C. Rau, Phil. Mag. 16, 663 (1967).

[7]D. T. Keating and A. N. Goland, Acta Met. 15, 1805 (1967).

[8]A. N. Goland and D. T. Keating, J. Phys. Chem. Solids 29, 785 (1968).

[9]J. Kakinoki and Y. Komura, Acta Cryst. 19, 137 (1965).

[10]J. Kakinoki, Acta Cryst. 23, 875 (1967).

[11]R. Sato, Acta Cryst. A25, 309 (1969).

[12]S. Lele, Acta Cryst. A25, 551 (1969).

[13]B. E. Warren, J. Appl. Phys. 32, 2428 (1961).

[14]J. W. Christian and J. Spreadborough, Proc. Phys. Soc. (London) B70, 1151 (1957).

[15]H. Holloway and M. S. Klamkin, J. Appl. Phys. 40, 1681 (1969).

[16]T. M. Sabine, J. Nucl. Mater. 14, 159 (1964).

[17]S. Lele, T. R. Anantharaman, and C. A. Johnson, Phys. Status Solidi 20, 59 (1967).

[18]M. A. Krivoglaz and K. P. Ryaboshapka, Phys. Met. Metallog. 16 (No. 5), 1 (1963).

[19]M. A. Krivoglaz, *Theory of X-Ray and Thermal-Neutron Scattering by Real Crystals* (Plenum, New York, 1969), p. 268.

[20]J. D. Eshelby, Proc. Roy. Soc. (London) A241, 376 (1957).

[21]D. T. Keating and A. N. Goland, J. Appl. Phys. 39, 6018 (1968). [Note omission of ξ in Eq. (1b) of this reference.]

[22]A. N. Goland and D. T. Keating, J. Appl. Phys. 41, 814 (1970).

[23]M. A. Krivoglaz, Phys. Met. Metallog. 7 (No. 5), 11 (1959).

[24]M. A. Krivoglaz, Ref. 19, p. 228ff.

[25]K. Huang, Proc. Roy. Soc. (London) A190, 102 (1947).

[26]J. D. Eshelby, J. Appl. Phys. 25, 255 (1954).

[27]J. R. Townsend, Acta Met. 13, 325 (1965).

[28]H. Ekstein, Phys. Rev. 68, 120 (1945).

[29]W. Cochran, Acta Cryst. 9, 259 (1956).

[30]W. Cochran and G. Kartha, Acta Cryst. 9, 941 (1956).

[31]W. Cochran and G. Kartha, Acta Cryst. 9, 944 (1956).

[32]D. T. Keating, J. Phys. Chem. Solids 29, 771 (1968).

[33]C. R. Hall, J. Phys. Chem. Solids 30, 919 (1969).

[34]D. T. Keating, J. Phys. Chem. Solids (to be published).

[35]F. Kroupa, Czech. J. Phys. B10, 284 (1960).

[36]M. Rühle, M. Wilkens, and U. Essmann, Phys. Status Solidi 11, 819 (1965).

[37]I. N. Sneddon, *Fourier Transforms* (McGraw-Hill, New York, 1951), Chap. 10.

[38]R. W. James, *The Optical Principles of the Diffraction of X-Rays* (G. Bell and Sons, London, 1950), p. 548.

[39]E. Jahnke and F. Emde, *Tables of Functions* (Dover, New York, 1945), pp. 128 and 181.

[40]D. T. Keating and A. N. Goland, Acta Cryst. A27, 134 (1971).

[41]J. Nucl. Mater. 14, 1–498 (1964).

[42]R. S. Wilks, J. Nucl. Mater. 26, 137 (1968).

[43]C. F. Cline, H. L. Dunegan, and G. W. Henderson, J. Appl. Phys. 38, 1944 (1967).

[44]D. G. Walker, R. M. Mayer, and B. S. Hickman, J. Nucl. Mater. 14, 147 (1964).

[45]R. C. Rau (private communication).

[46]D. T. Keating and B. E. Warren, Rev. Sci. Instr. 23, 519 (1952).

[47]J. J. Millar and Z. Barnea, J. Phys. E 3, 571 (1970).

[48]J. J. Millar (private communication).

[49]R. W. G. Wyckoff, *Crystal Structure* (Interscience, New York, 1960), Suppl. to Vol. I, Chap. III, table on p. 42C.

[50]R. C. Rau, S. F. Bartram, and K. Lacefield, J. Am. Ceram. Soc. 48, 233 (1965).

[51]S. B. Austerman and K. T. Miller, Phys. Status Solidi 11, 241 (1965).

[52]B. Belbéoch, J. Rodot, and M. Roulliary, J. Nucl. Mater. 15, 234 (1965).

[53]B. Belbéoch, J. Rodot, and M. Roulliary, Centre D'Etudes Nucleaires De Saclay Rapport CEA-R 2943, 1966 (unpublished).

[54]B. Belbéoch (private communication).

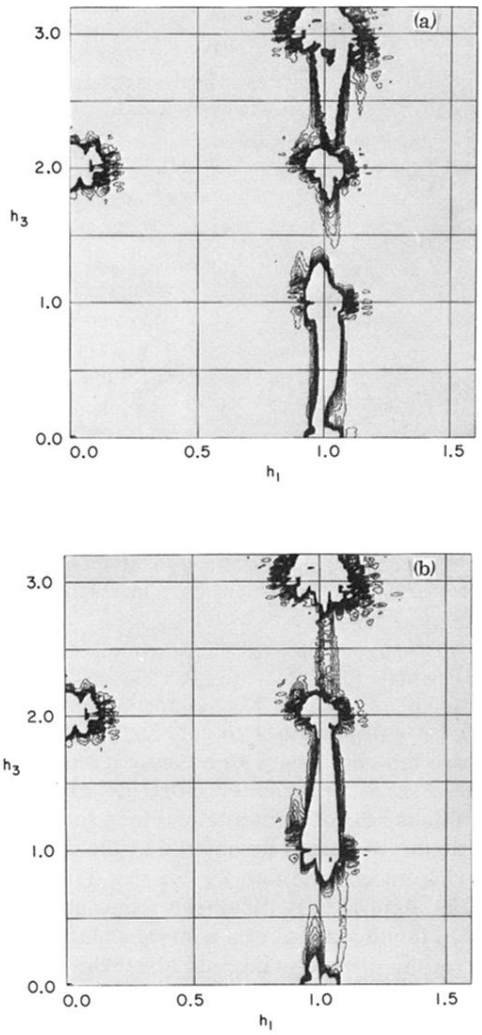

FIG. 10. (a) Isodiffuse intensity contours in h_1, 0, h_3 plane from *AB* loops. Note the absence of the $(00 \cdot L)$ rod and the strengthening of the diffuse bridge between $(10 \cdot 0)$ and $(10 \cdot 1)$. (b) Same as (a) but for *BA* loops. Note absence of an $(00 \cdot L)$ rod and diffuse bridge between $(10 \cdot 1)$ and $(10 \cdot 2)$. Contours are the same as in Fig. 9.

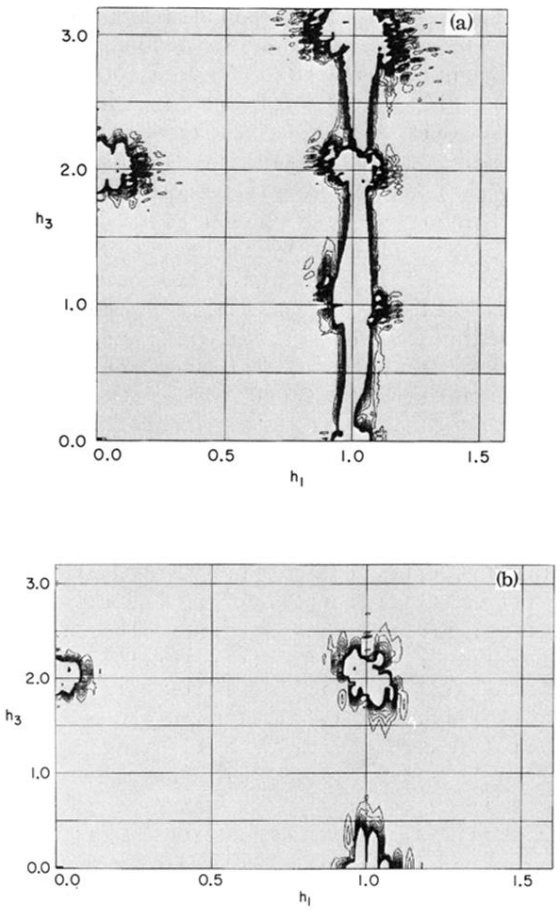

FIG. 11. (a) Isodiffuse intensity contours in the h_1, 0, h_3 plane for both AB and BA loops. Note absence of the $(00 \cdot L)$ rod and the presence of the $(10 \cdot L)$ rod. (b) Same as (a) but in the h_1, h_1, h_3 plane. Note absence of rods and the diffuse scattering localized in the vicinity of the Bragg reflections. The contours are the same as in Fig. 9.

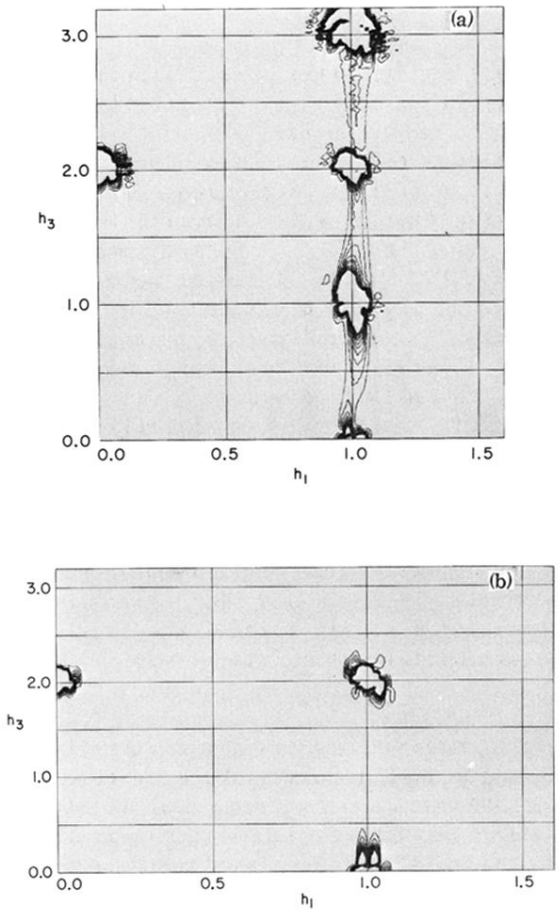

FIG. 12. Same as Fig. 11 but here there are 10 contours with a contour interval of 50 000.

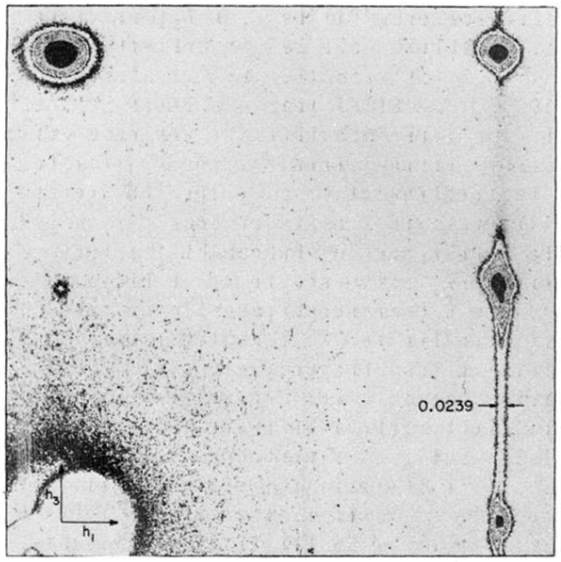

FIG. 15. Isodensitracing of a precession photograph of the h_1, 0, h_3 plane in the reciprocal space of a neutron-irradiated BeO crystal. The exposure is 2.1×10^{20} n/cm^2 ($E \geq 1$ MeV). Compare the figure to Figs. 11(a) and 12(a). From the width of the $(10 \cdot L)$ rod indicated, the loops contain ~ 1260 BeO molecules. The weakness of the rod between $(10 \cdot 1)$ and $(10 \cdot 2)$ is due to the destructive interference between Be and O.

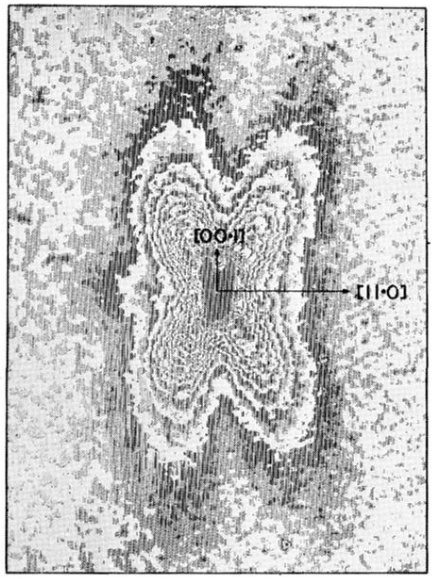

FIG. 17. Isodensitracing of an oscillation photograph of a neutron-irradiated BeO crystal. The exposure is 2.0×10^{20} n/cm^2 ($E\geq1$ MeV). The angle of oscillation is 2.5° on both sides of the (11·0) and the axis of rotation is (00·1). Compare the figure to Figs. 11(b) and 12(b).

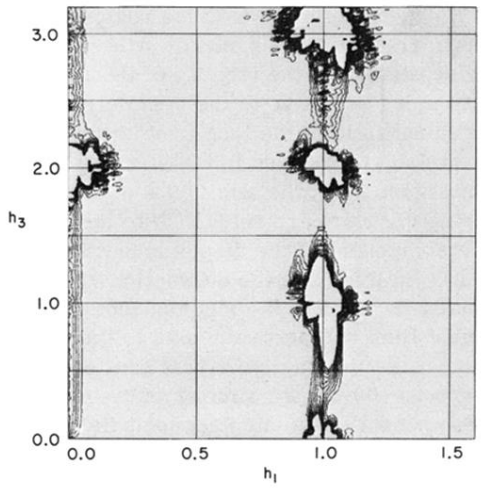

FIG. 9. Isodiffuse intensity contours in h_1, 0, h_3 plane from only the displacements produced by an AB loop. Note the $(00 \cdot L)$ rod and the diffuse bridge between $(10 \cdot 0)$ and $(10 \cdot 1)$. There are 10 contours and the interval is 5000.